



Final Draft **of the original manuscript**

Zhang, X.; Lutz, A.; Andrä, H.; Lahres, M.; Gan, W.; Maawad, E.; Emmelmann, C.:

Evolution of microscopic strains, stresses, and dislocation density during in-situ tensile loading of additively manufactured AlSi10Mg alloy.

In: International Journal of Plasticity. Vol. 139 (2021) 102946.

First published online by Elsevier: 01.02.2021

<https://dx.doi.org/10.1016/j.ijplas.2021.102946>

Evolution of microscopic strains, stresses, and dislocation density during in-situ tensile loading of additively manufactured AlSi10Mg alloy

X.X. Zhang^{1,*}, A. Lutz², H. Andrä¹, M. Lahres², W.M. Gan³, E. Maawad³, C. Emmelmann⁴

¹ *Fraunhofer Institute for Industrial Mathematics ITWM, Fraunhofer-Platz 1, 67663 Kaiserslautern, Germany*

² *Mercedes Benz AG, Research and Development Department, Leibnizstraße 2, 71032 Böblingen, Germany*

³ *Institute of Materials Research, Helmholtz-Zentrum Geesthacht, Max-Planck-Str. 1, 21502 Geesthacht, Germany*

⁴ *Institute of Laser and System Technologies, Hamburg University of Technology (TUHH), Am Schleusen graben 14, 21029 Hamburg, Germany*

Abstract

The AlSi10Mg alloy produced by laser powder bed fusion (LPBF) possesses a novel microstructure and higher mechanical properties compared with its casting counterpart. So far, the crystallographic orientation-dependent lattice strains, average phase stresses, and dislocation density during the tensile loading of the LPBF AlSi10Mg are not well understood. This fact is impeding further optimization of microstructure and mechanical properties. High energy synchrotron X-ray diffraction providing deep penetration capability and phase-specific measurements of various bulk properties of crystal materials is applied to investigate the LPBF AlSi10Mg under loading. The crystallographic orientation-dependent lattice strains and elastoplastic properties of the Al matrix are assessed. The average phase stresses are calculated to quantify load partitioning between the Al and Si phases. The nano-sized Si particles that bear high-stress are efficient strengthening particles. The maximum value of the average phase stress of Si reaches up to ~2 GPa. Based on the modified Williamson-Hall and the modified Warren-Averbach methods, the dislocation density and its evolution during the plastic deformation are determined. A multistage strain hardening behavior is detected in the Al matrix, which is associated with the interactions between the dislocations and the cell boundary network.

Keywords: In-situ synchrotron X-ray diffraction (SXRD); laser powder bed fusion (LPBF); load partitioning; dislocation density; strain hardening behavior; aluminum alloy

*Corresponding author. Present address: Heinz Maier-Leibnitz Zentrum (MLZ), Technical University of Munich, Lichtenbergstrasse 1, 85748 Garching, Germany; Tel.: +49-89-28954865; E-mail: Xingxing.Zhang@frm2.tum.de

1. Introduction

The transformation towards emission-free, individual or shared mobility solutions in the automotive and aerospace industries leads to rising demand for high strength-to-weight ratio parts with optional customization possibilities. Over the last years, additive manufacturing (AM) techniques have advanced to obtain high and reliable quality, and thus these techniques can be used to create end-use parts (Aboulkhair et al., 2019; Herzog et al., 2016; Olakanmi et al., 2015). Aluminum alloys with a beneficial strength-to-weight ratio are extensively used in the automotive and aerospace industries. Among them, the well-known cast alloy AlSi10Mg is particularly suitable for laser powder bed fusion (LPBF), a promising AM route, due to the good cast-ability, low shrinkage, superior hot tearing, and corrosion resistance (Kempen et al., 2012; Thijs et al., 2013). Nevertheless, the LPBF AlSi10Mg alloy also shows relatively low ductility, partially due to the presence of a non-negligible amount of porosity (Samei et al., 2019). By optimizing the process parameters and scan strategies, the porosity can be minimized, and a high relative-density of 99.8% has been achieved (Aboulkhair et al., 2014).

LPBF, with its local melting of powders at extremely high heating and cooling rates ($\sim 10^5$ - 10^6 K/s (Aboulkhair et al., 2019)), leads to a novel microstructure entirely different from those of common manufacturing strategies, e.g. casting or forging. The LPBF AlSi10Mg alloy consists of a hierarchical, heterogeneous, and fine microstructure typically containing three-level networks: the melt pool boundary network (Trevisan et al., 2017), the grain boundary network (Chen et al., 2017; Wu et al., 2016), and the cell boundary network (Chen et al., 2017; Delahaye et al., 2019; Li et al., 2020; Wu et al., 2016).

Under proper conditions, the LPBF AlSi10Mg alloy with the sophisticated microstructure possesses superior mechanical properties compared with its casting counterpart, as shown in Table 1. Several mechanisms lead to its high performance. For instance, it benefits from grain refinement of the Al matrix. The fine Si precipitates and eutectic cell-boundaries impede dislocation motions (Chen et al., 2017). The thermal mismatch between the Al and Si phases generates many dislocations in the Al matrix (Wu et al., 2016). Among these mechanisms, dislocations and their interaction with obstacles have been characterized by transmission electron microscopy (TEM) (Chen et al., 2017; Wu et al., 2016).

Nevertheless, Table 1 reveals that the mechanical properties of AlSi10Mg manufactured under different process conditions vary significantly. Such variability involves a high risk of producing reliable components for industrial applications. Further tailoring the mechanical

properties requires a deep understanding of the micromechanical behavior. For multiphase alloys like AlSi10Mg, the load partitioning at the grain and phase scale governs the load-bearing capacity of the alloys (Harjo et al., 2017a; Kim et al., 2017). Moreover, the deformation incompatibilities between different grains and phases have remarkable impacts on the ductility (Hong et al., 2018; Nguyen et al., 2019). Therefore, clarifying the lattice strains and average phase stresses at the grain and phase scale can provide valuable insights.

Synchrotron X-ray diffraction (SXRD) and neutron diffraction have been essential techniques to investigate the statistical information (e.g. phase content, lattice strain, average phase stress, texture, and dislocation density) of the crystalline materials in a non-destructive way, because of their deep penetration capability and phase-specific measurements (Withers, 2004). In-situ SXRD and neutron diffraction experiments under various loading conditions have been achieved successfully in Al alloys (Davidson et al., 2017; Xie et al., 2020), Fe alloys (Harjo et al., 2017a; Kim et al., 2019), TiAl alloy (Erdely et al., 2018), et cetera. For the LPBF AlSi10Mg alloy, the previous research by Kim et al. (Kim et al., 2017) has investigated the average phase stresses via in-situ neutron diffraction and crystal plasticity modeling. Nevertheless, the crystallographic orientation-dependent elastoplastic deformation and the dislocation density of the Al matrix in the LPBF AlSi10Mg are not addressed. Hence, further in-depth investigation of the LPBF AlSi10Mg alloy is deserved.

The mechanical properties of multiphase alloys are linked not only to the load partitioning and deformation incompatibilities but also to the dislocations (Jiang et al., 2019; Liu et al., 2020; Srinivas and Panigrahi, 2020; Yang et al., 2018). In this respect, the investigation of the dislocation behavior is fundamental to understand the strength and ductility of the LPBF AlSi10Mg. TEM is a common technique to characterize dislocations. For instance, it has been found out that dislocation pile-ups form in the Al matrix near the eutectic cell boundaries (Kim et al., 2017; Li et al., 2020). Besides, the dislocation loops can arise in the Al matrix around the Si particles (Chen et al., 2017). Moreover, in-situ TEM characterization has revealed that the eutectic cell boundaries inhibit the dislocation motions in the LPBF AlSi10Mg (Wu et al., 2016). Although the previous qualitative TEM observations provide a lot of useful information, lacking quantitative in-situ measurement of the dislocations in the LPBF AlSi10Mg during loading hampers further analysis and optimization of the ductility. The relation between the dislocations and strain hardening behavior introduced by the unique microstructure remains unknown, which requires a detailed analysis.

In the present work, the micromechanical behavior of the LPBF AlSi10Mg alloy was

investigated via in-situ SXR, including dynamic developments of texture, lattice strains, average phase stresses, and dislocation density during tensile deformation. Load partitioning and deformation incompatibility among Al grain families with different crystallographic orientations were ascertained. The evolution of dislocation density in the Al matrix during in-situ loading is evaluated based on the modified Williamson-Hall (mWH) (Ungar et al., 1999) and the modified Warren-Averbach (mWA) (Arechabaleta et al., 2016; Sahu et al., 2012; Ungar et al., 1998) methods. Afterward, the strain hardening behavior at the microscale is assessed. The microstructures were examined using both optical microscopy (OM) and transmission electron microscopy (TEM). Further relations between the microstructures, micromechanical behavior, and macroscopic properties were established. This work provides an in-depth insight into the LPBF AlSi10Mg alloy, which helps researchers to develop high-performance LPBF end-use parts. Meanwhile, the present experimental investigation lays the foundation for developing multiscale models of additively manufactured Al alloys.

2. Experimental procedures and methodology

2.1 Material and LPBF process

The considered rod specimens of the AlSi10Mg alloy were printed horizontally via an LPBF method. The chemical composition of the AlSi10Mg powder (conforming to DIN EN 1706) is listed in Table 2. A Concept Laser M2 cusing laser system was utilized with a laser power of 370 W and a laser spot diameter of 150 μm . The scanning speed was set to 1500 mm/s, and the layer thickness was 30 μm . The hatch distance was 105 μm , and no pre-heating of the build platform was applied. The powders had a particle size range of 20-63 μm .

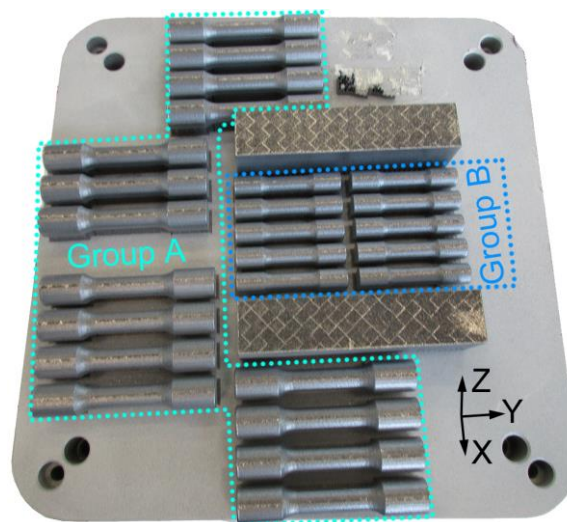


Fig. 1 As-built specimens of the LPBF AlSi10Mg alloy.

The as-built specimens and base plate are shown in Fig. 1. Group A specimens were machined to the final shape with a total length of 76 mm, whose geometry is shown in Fig. 2(a). Group B specimens were machined to the final shape with a total length of 50 mm, whose geometry is shown in Fig. 2(b). The thickness of the removed surface during machining was about 1.5-1.8 mm for the center parallel parts of all rod specimens. All specimens were tested in the as-built plus machining condition without heat treatment.

2.2 Ex-situ tensile tests

The ex-situ tensile tests were performed on a uniaxial electro-mechanical testing rig of type Zwick Z50. Three specimens (namely E1, E2, and E3) were tested at room temperature with a nominal strain rate of $1.5 \times 10^{-4} \text{ s}^{-1}$. The specimen geometry is shown in Fig. 2(a). The strain until breakage was measured with a high accuracy extensometer.

2.3 Microstructure characterization

The OM characterization of the threaded part of the rod specimen was performed on a Zeiss Axio Imager M2 microscope. The etched samples were immersed in a solution containing 85 vol.% distilled water, 5 vol.% HF, and 10 vol.% H₂SO₄ for 5 s. Besides, the OM characterization of the center parallel part of the rod specimen was performed on a Zeiss Axio Scope.A1 microscope.

High-resolution TEM (HRTEM) analysis was conducted on a Jeol ARM200 with a Cs corrector at an accelerating voltage of 200kV. The scanning mode (STEM) with the annular dark field detector and the Jeol Dual EDX (energy-dispersive X-ray) system was utilized for element mapping. The sample was cut from an undeformed section using a focused ion beam. The direction of transmission is perpendicular to the XY plane.

2.4 In-situ SXR D experiment

The in-situ SXR D experiment was conducted at the side station of the High Energy Materials Science (HEMS) beamline P07B operated by the Helmholtz-Zentrum Geesthacht at PETRA III, DESY. Fig. 2(b) shows the geometry of the rod specimens for the in-situ tensile experiment, and Fig. 2(c) illustrates the SXR D experimental setup.

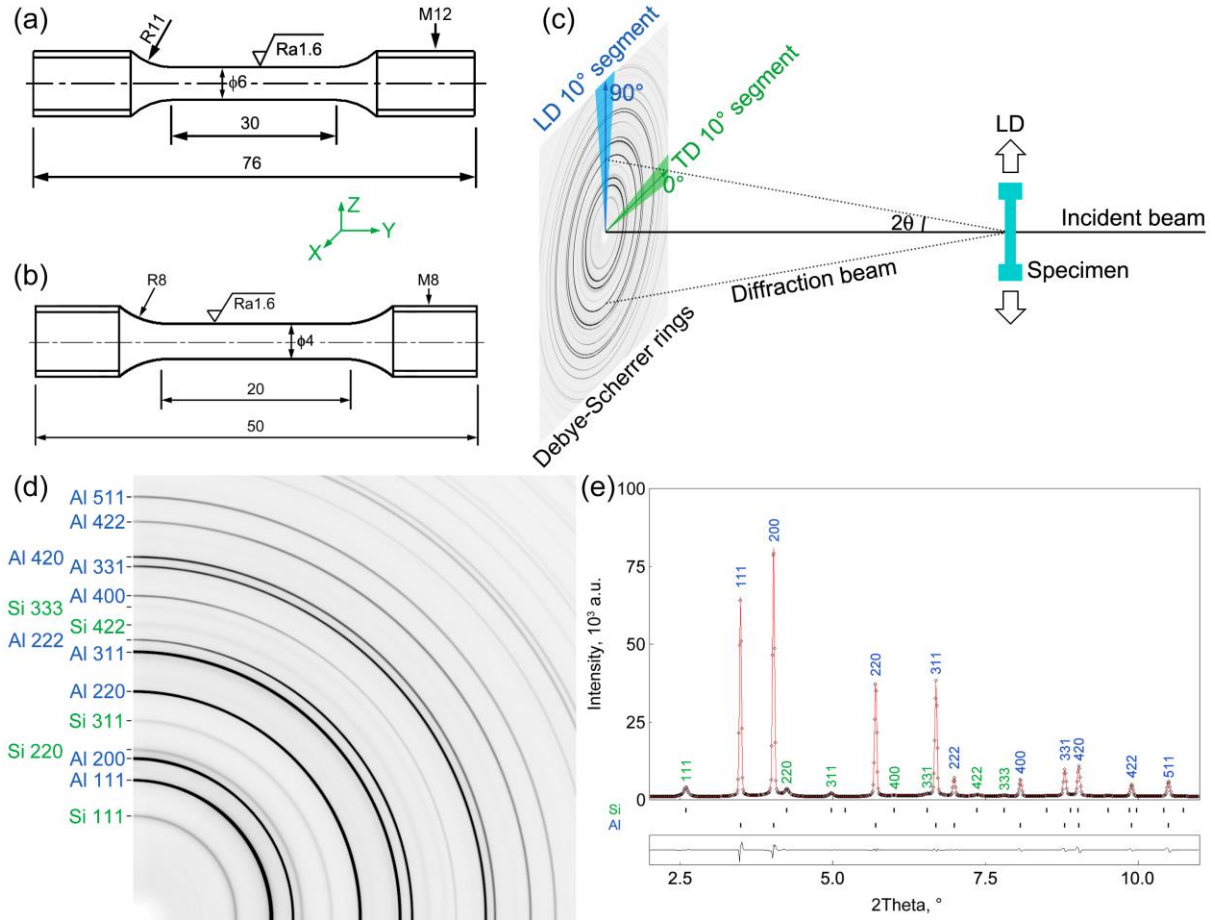


Fig. 2 Experimental aspects: geometry of the (a) ex-situ and (b) in-situ tensile specimens (unit in mm); (c) schematic representation of the SXR D experimental setup; (d) a quarter of 2D diffraction image; (e) the corresponding intensity- 2θ diffraction spectrum, where the Al and Si peaks are marked, and the fitting residual is shown at the bottom. The empty black rhombuses in (e) denote the measured data, and the red line shows the fitted pattern.

Two LPBF AlSi10Mg specimens were tested using a load frame located on the sample table. The crosshead displacement rate was 0.003 mm/s, resulting in a strain rate of $1.5 \times 10^{-4} \text{ s}^{-1}$. Specimen 1 (S1) was subjected to a continuously uniaxial tensile test to measure the strains, stresses, and dislocation density. Specimen 2 (S2) was subjected to a uniaxial tensile test to measure the texture. The crosshead was paused at target values under a displacement control mode for texture measurement. Then the sample table rotated around the loading direction (LD) from -70° to 70° . Diffraction patterns were collected at every 2.5° . The position where the incident X-ray beam passed through the specimen was marked on the round surface of S2. Afterward, the angle between the incident X-ray and the printing layers was checked via OM to define a reference coordinate system for texture characterization.

The wavelength of the synchrotron X-ray was 0.14235 Å, corresponding to X-ray energy of 87.109 keV. An incident beam size of 0.7×0.7 mm² was used, resulting in a diffraction volume of 0.7×0.7×4.0 mm³. A Perkin Elmer XRD 1622 flat panel detector with 2048×2048 pixels and a pixel size of 200×200 μm² was utilized for diffraction pattern acquisition. The specimen-to-detector distance was 993.8 mm as calibrated using a LaB₆ powder standard. The specimen-to-detector distance was the same for all the in-situ measurements.

2.5 Fitting of two-dimensional diffraction images

The 10° cake segments at positions of 0° ± 5° (right) and 90° ± 5° (up) were used to calculate the intensity-2θ diffraction spectrums for the transverse direction (TD) and LD, respectively, see Fig. 2(c). The 10° cake segments at positions of 180°±5° (left) and 270°±5° (down) were also used for the TD and LD, respectively, to improve the counting statistics and minimize the influence of fitting uncertainties. Fig. 2(d) shows a quarter of a diffraction pattern, and Fig. 2(e) shows an intensity-2θ diffraction spectrum.

2.6 Texture analysis

The incomplete pole figures of Al {111}, {200}, and {220} were calculated using software StressTextureCalculator (Randau et al., 2011). The orientation distribution functions (ODFs) were then calculated based on the pole figures using the iterative series expansion method with $L_{\max} = 20$.

2.7 Analysis of crystallographic orientation-dependent strains

The {hkl} lattice strain $\varepsilon_{hkl}^{i,s}$ in phase i ($i = \text{Al}$ or Si) along direction s ($s = \text{LD}$ or TD) is calculated by the equation

$$\varepsilon_{hkl}^{i,s} = \frac{\sin \theta_{hkl,0}^{i,s}}{\sin \theta_{hkl}^{i,s}} - 1, \quad (1)$$

where the angle $\theta_{hkl}^{i,s}$ is the peak position, subscript 0 denotes the reference condition.

The {hkl} diffraction elastic modulus (DEM) E_{hkl}^i of phase i can be determined by

$$E_{hkl}^i = \frac{\partial \sigma_{i,\text{LD}}}{\partial \varepsilon_{hkl}^{i,\text{LD}}}, \quad (2)$$

where $\sigma_{i,\text{LD}}$ is the stress of phase i in the LD, $\varepsilon_{hkl}^{i,\text{LD}}$ the lattice strain of phase i in the LD. However, as the average phase stress cannot be measured directly, the normalized {hkl} DEM of each phase is determined in the present study. Since the {111} DEM of the face-centered

cubic (FCC) crystals is the stiffest (Clausen et al., 1998), the $\{hkl\}$ DEM of the Al and Si phases along the LD is normalized based on the $\{111\}$ DEM by

$$E_{hkl}^{i,\text{norm}} = \frac{E_{hkl}^{i,\text{LD}}}{E_{111}^{i,\text{LD}}} = \frac{\sigma_{i,\text{LD}}/\varepsilon_{hkl}^{i,\text{LD}}}{\sigma_{i,\text{LD}}/\varepsilon_{111}^{i,\text{LD}}} = \frac{\varepsilon_{111}^{i,\text{LD}}}{\varepsilon_{hkl}^{i,\text{LD}}}, \quad (3)$$

2.8 Analysis of phase strains and stresses

Rietveld refinement uses all measured peaks, and it is capable of providing average phase strains, which represent the macroscopic strains of each phase. Here, all diffraction spectrums were analyzed by Rietveld refinement carefully to obtain the average lattice parameter $a^{i,s}$ for phase i in direction s using MAUD (MAUD, 2019). For the Rietveld refinement analysis, the Delft type line broadening model (Dekeijser et al., 1982) and the arbitrary texture model were selected. Hence, the line broadening and deformation texture effects during the plastic deformation can be captured to minimize the fitting uncertainty. Based on the refined $a^{i,s}$ values, the average phase strain $\varepsilon_{i,s}$ is calculated by

$$\varepsilon_{i,s} = \frac{a^{i,s}}{a_0^{i,s}} - 1, \quad (4)$$

where $a_0^{i,s}$ is the reference lattice parameter.

Assuming both the Al and Si phases experience uniaxial stress state, the Poisson's ratio ν_i of phase i can be measured by

$$\nu_i = -\frac{\varepsilon_{i,\text{TD}}}{\varepsilon_{i,\text{LD}}}, \quad (5)$$

where $\varepsilon_{i,\text{TD}}$ and $\varepsilon_{i,\text{LD}}$ are average phase strains in the elastic stage.

The triaxial average phase stresses can be calculated from the average phase strains based on the general Hooke's law

$$\sigma_{i,\text{LD}} = A_i \left[B_i \varepsilon_{i,\text{LD}} + \nu_i (\varepsilon_{i,\text{TD}} + \varepsilon_{i,\text{ND}}) \right], \quad (6)$$

$$\sigma_{i,\text{TD}} = A_i \left[B_i \varepsilon_{i,\text{TD}} + \nu_i (\varepsilon_{i,\text{LD}} + \varepsilon_{i,\text{ND}}) \right], \quad (7)$$

$$\sigma_{i,\text{ND}} = A_i \left[B_i \varepsilon_{i,\text{ND}} + \nu_i (\varepsilon_{i,\text{LD}} + \varepsilon_{i,\text{TD}}) \right], \quad (8)$$

where $A_i = E_i \left[(1 + \nu_i)(1 - 2\nu_i) \right]^{-1}$, $B_i = 1 - \nu_i$, E_i is the Young's modulus of phase i , and ν_i the Poisson's ratio of phase i . In Eqs. (6)-(8), the average phase strain in the normal direction (ND) $\varepsilon_{i,\text{ND}}$ is required, but it is not available because in-situ SXRD or neutron diffraction only measures $\varepsilon_{i,\text{LD}}$ and $\varepsilon_{i,\text{TD}}$.

Two methods are often adopted to calculate the average phase stress to overcome the above problem. The first method (M1) assumes $\sigma_{i,\text{TD}} = \sigma_{i,\text{ND}} = 0$, so the stress in the LD for phase i $\sigma_{i,\text{LD}}$ is calculated simply by (Harjo et al., 2017b; Van Petegem et al., 2016)

$$\sigma_{i,\text{LD}} = E_i \varepsilon_{i,\text{LD}}. \quad (9)$$

The second method (M2) assumes $\varepsilon_{i,\text{ND}} = \varepsilon_{i,\text{TD}}$. Then the average phase stresses can be calculated by Eqs. (6)-(8).

2.9 Determination of dislocation density

Both the mWH and mWA methods were employed to determine the dislocation density in the Al matrix (Arechabaleta et al., 2016; Sahu et al., 2012; Ungar et al., 1998). The LaB₆ powder standard was measured to calibrate the instrumental broadening. The heterogeneous strains could also contribute to the peak broadening slightly for the Al matrix. Although it is difficult to subtract this effect quantitatively, it is small compared with the peak broadening caused by dislocation multiplication during plastic deformation for the Al matrix. Therefore, the heterogeneous strain effect is not considered (Arechabaleta et al., 2016; Bahl et al., 2017; Harjo et al., 2020; Sahu et al., 2012; Ungar et al., 1998).

The physical full width at half maximum (FWHM) β_{phy} was determined from the following equation (Sallez et al., 2015)

$$\beta_{\text{raw}}^2 = \beta_{\text{phy}} \beta_{\text{raw}} + \beta_{\text{ins}}^2, \quad (10)$$

where β_{raw} and β_{ins} are the FWHM of the diffraction spectrums of the LPBF AlSi10Mg and LaB₆ specimens, respectively. Here, β_{raw} , β_{phy} and β_{ins} are defined in the K space, with a unit of nm⁻¹. The diffraction vector K is defined by $K = 2 \sin \theta / \lambda$, with θ and λ being the diffraction angle and the wavelength of X-ray.

The mWH function of the physical FWHM β_{phy} reads (Ungar et al., 1999)

$$\beta_{\text{phy}} = 0.9/D + (\pi M^2 b^2 / 2)^{1/2} \rho^{1/2} (KC^{1/2}) + O(K^2 C), \quad (11)$$

where D is the average crystal size, M a material constant depending on the effective outer cut-off radius of dislocations R_e and the dislocation density ρ , b the magnitude of the Burgers vector, C the average contrast factor, and $O(K^2 C)$ represents higher-order terms. The average contrast factor C is calculated by

$$C = \bar{C}_{h00} (1 - qH^2), \quad (12)$$

$$H^2 = \frac{h^2k^2 + h^2l^2 + k^2l^2}{(h^2 + k^2 + l^2)^2}, \quad (13)$$

where \bar{C}_{h00} is the average dislocation contrast factor for the ($h00$) reflection, and q a parameter depending on the edge or screw character of dislocations. The q value can be determined as the intercept of the $\left[\beta_{\text{phy}}^2 - (0.9/D)^2\right]/K^2$ vs. H^2 line with the H^2 axis (Arechabaleta et al., 2016; Sahu et al., 2012).

The basic function of the mWA method is expressed as (Arechabaleta et al., 2016; Sahu et al., 2012; Ungar et al., 1998):

$$\ln A_L = \ln A_L^S - \rho BL^2 \ln(R_e/L)(K^2C) + QB^2L^4 \ln(R_1/L)\ln(R_2/L)(K^2C)^2, \quad (14)$$

where A_L is the real part of the Fourier coefficients, A_L^S the size Fourier coefficients, $B = \pi b^2/2$, Q the correlation factor, L the Fourier length, R_1 and R_2 are auxiliary constants. The instrumental contributions to the Fourier coefficients were subtracted using the Stokes method (Stokes, 1948; Wang and Huang, 2020; Zhong et al., 2007). By fitting $\ln A_L$ as a quadratic function of K^2C for different L values, the coefficient of the second term on the right-hand side of Eq. (14), denoting by $X(L) = \rho BL^2 \ln(R_e/L)$, can be obtained. Then, the dislocation density ρ can be determined from the linear regression using (Arechabaleta et al., 2016; Sahu et al., 2012):

$$X(L)/L^2 = \rho B(\ln R_e - \ln L). \quad (15)$$

3. Results and discussions

3.1 Macroscopic mechanical properties and microstructure

The true stress-strain curves of different specimens are shown in Fig. 3(a). The curves of LPBF and powder metallurgy (PM) AlSi10Mg alloys from (Chen et al., 2017) are compared here. The present LPBF AlSi10Mg possesses higher tensile strength and more significant strain hardening behavior, which is analyzed in sections 3.4 and 3.7. Meanwhile, the present LPBF AlSi10Mg alloy exhibits much higher strength and lower elongation than the PM counterpart. For S2, the tensile test was paused under a displacement control mode to measure the texture. A typical stress relaxation effect causes stress drops along the S2 true stress-strain curve (Song et al., 2017; Wang et al., 2016). The mechanical properties obtained from the in-situ and ex-situ tests are summarized in Table 3. The yield strength, tensile strength, and elongation obtained from the ex-situ tests are 301.0 ± 6.5 MPa, 495.7 ± 8.7 MPa, and $7.0 \pm 0.5\%$, respectively.

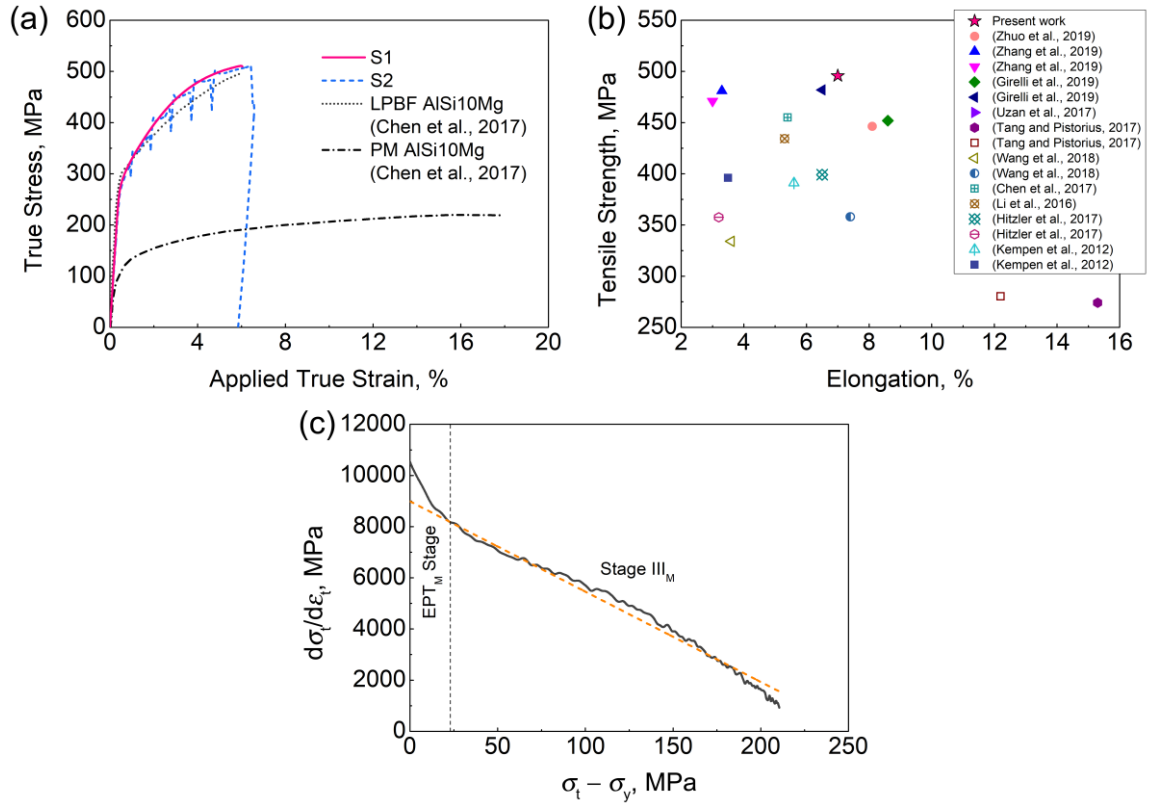


Fig. 3 Macroscopic mechanical properties of the AlSi10Mg alloy: (a) true stress-strain curves of S1, S2, LPBF and PM AlSi10Mg alloys from literature (Chen et al., 2017); (b) tensile strengths and elongations of the LPBF AlSi10Mg alloy from different references and the present work; (c) macroscopic Kocks–Mecking plot of S1, where the yellow dash line is a linear regression of stage III_M, with the subscript _M denoting macroscopic.

The mechanical properties of the LPBF and cast AlSi10Mg alloys from previous investigations are summarized in Table 1. Besides, the tensile strengths and elongations of the LPBF AlSi10Mg alloy from different references and the present work are compared in Fig. 3(b). It can be seen that the present LPBF AlSi10Mg alloy shows a very good combination of strength and ductility. It should be mentioned that the mechanical properties of LPBF alloys are affected by many process parameters, as summarized by Aboulkhair et al. (Aboulkhair et al., 2019), which at least include laser-related parameters (e.g. laser power, spot size, and pulse duration), scan-related ones (e.g. scan speed, spacing, and pattern), powder-related ones (e.g. particle size and shape, powder bed density, and material properties), and temperature-related ones (e.g. powder bed temperature and temperature uniformity). Hence, further optimization of process parameters to get high quality is possible.

The macroscopic Kocks–Mecking plot (Kocks and Mecking, 2003) of S1 in Fig. 3(c)

reveals that the strain hardening behavior of the LPBF AlSi10Mg includes the macroscopic elastoplastic transition (EPT_M) stage and stage III_M , which is similar to the previous report (Chen et al., 2017). The EPT_M stage is characterized by a high strain hardening rate in polycrystalline metals and alloys. The stage III_M corresponds to the deformation region, where the strain hardening rate decreases linearly with flow stress or value of “flow stress – yield strength” (Kocks and Mecking, 2003). S1 fractured before necking. At the fracture point, the hardening coefficient $d\sigma_1/d\varepsilon_1$ is ~ 876 MPa (Fig. 3(c)), much higher than the corresponding true stress of ~ 511 MPa (Fig. 3(a)).

Fig. 4(a) indicates that the distribution of pores is homogeneous in general. A typical polished and un-etched OM microstructure (with a magnification factor of 25x) in Fig. 4(b) shows the pores in detail. Two OM images with a magnification factor of 25x were obtained from the threaded part of the tensile specimen, from which the determined porosity is $0.13\pm 0.01\%$. In this case, one pixel in an OM image denotes $2.9\ \mu\text{m}$. Hence, the pores with diameters smaller than this resolution cannot be determined. Besides, 30 OM images with a magnification factor of 50x were obtained from six different locations of the center parallel part of the tensile specimen, from which the measured porosity is $0.12\pm 0.05\%$. In such a case, one pixel in an OM image represents $1.5\ \mu\text{m}$. The low porosity of the present LPBF AlSi10Mg alloy contributes to its high strength. Microstructures with higher magnification in Figs. 4(c) and (d) show typical inhomogeneity, where the melt pool network and heat-affected zones with relatively coarse dendrites are visible.

The STEM high-angle annular dark-field microstructure in Fig. 5 shows that the average diameter of the generally equiaxed Al cells is about $454\ \text{nm}$, which is much smaller than the grain size (Chen et al., 2017; Zhang et al., 2021). In an accompanying study (Zhang et al., 2021), the grain size of the LPBF AlSi10Mg alloy that is from the same manufacturing batch has been examined, which is $8.21\pm 5.48\ \mu\text{m}$ and close to the ones in the references (Chen et al., 2017; Takata et al., 2017). In addition, the EDX element maps confirm that the Si phase mainly exists in the eutectic cell boundary network, in agreement with the previous report (Hadadzadeh et al., 2018b). The Mg element is mainly dissolved into the Al matrix and concentrated slightly in the eutectic network, which may be resulted from intermetallic phases (Hadadzadeh et al., 2018b).

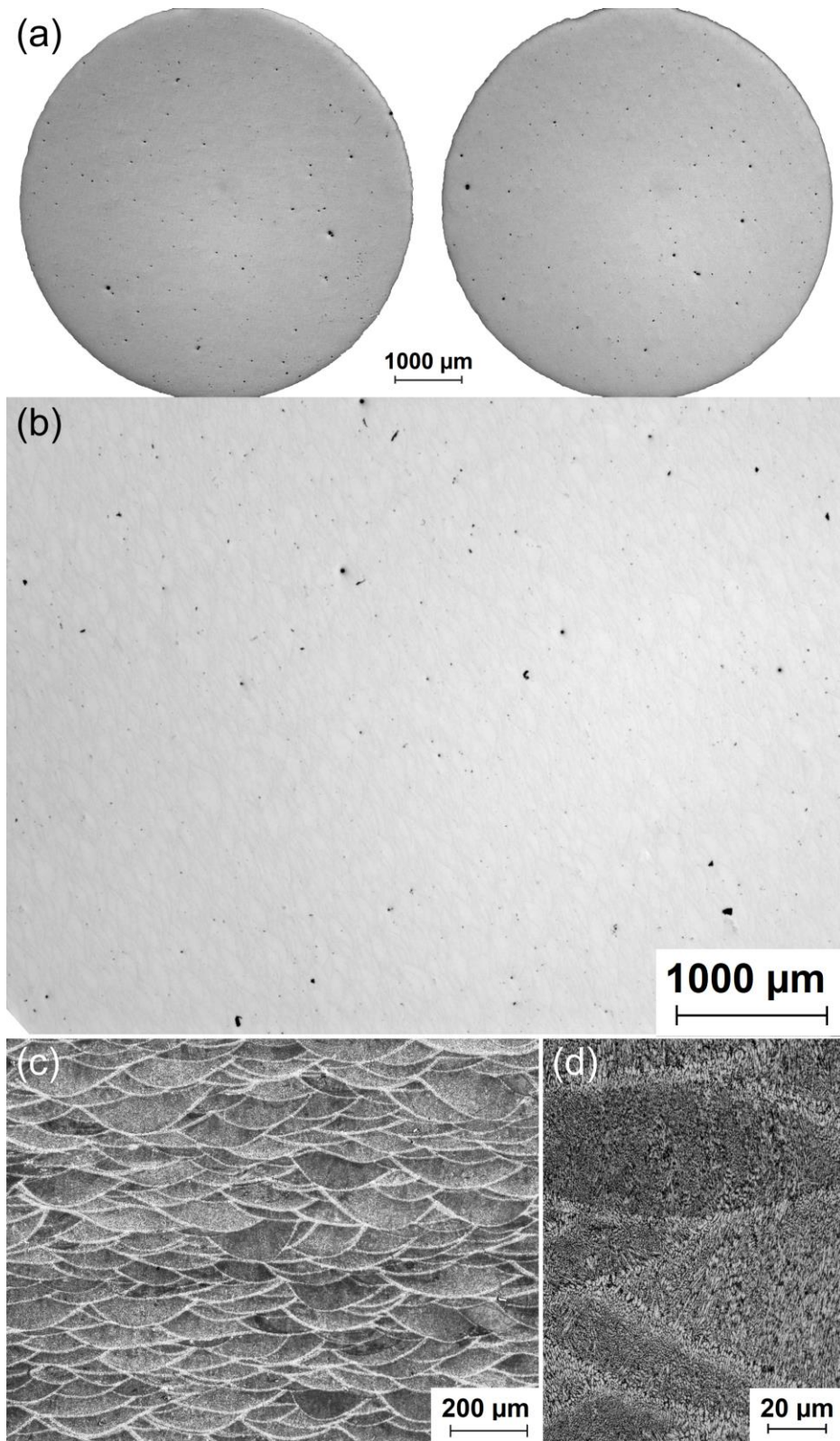


Fig. 4 OM microstructures of the as-built AlSi10Mg: (a) cross-sections of the un-deformed tensile specimen at different locations; (b) a typical polished and un-etched microstructure; (c) melting pools and laser traces, polished and etched; (d) higher magnification, polished and etched.

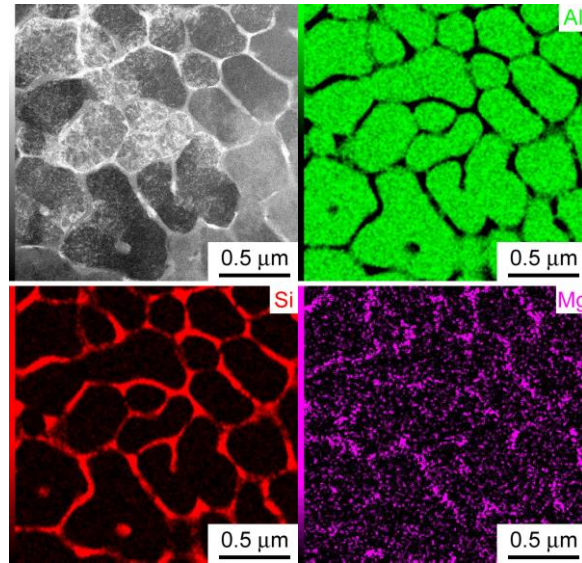


Fig. 5 STEM high-angle annular dark-field microstructure parallel to the XY plane along with EDX maps of Al, Si, and Mg elements.

The Si content and particle size in the eutectic phase were examined. The maximum Si contents in the eutectic boundaries along lines L1 and L2 in Fig. 6(a) are 32 at.% and 19 at.%, respectively, while the contents of other elements are very small. Therefore, the primary second phase in the eutectic boundaries is Si, as expected. Fig. 6(b) shows that the Si particles have a diameter range of about 10-30 nm. These nano-sized Si particles introduce significant Orowan strengthening (Chen et al., 2015). The content of the Si phase was analyzed via Rietveld refinement of the SXRD spectrums in the LD and TD. The average Si content is 8.40 wt.% (9.63 vol.%). This value coincides with the reference (Maamoun et al., 2019), where the Si content in the LPBF AlSi10Mg alloy is in the range of 8.02-9.19 wt.%. The Si particles with this high content also lead to significant strengthening due to the load transfer effect, which will be analyzed in detail in sections 3.3 and 3.4. No Mg_2Si phase is detected in this study and the reference (Maamoun et al., 2019).

The microstructure observations reveal that the good mechanical properties of the present LPBF AlSi10Mg alloy are caused by (a) a low porosity, (b) the small-sized grains (Zhang et al., 2021), (c) the nano-sized Si particles introducing Orowan strengthening, (d) the significant load transfer effect, and (e) a good strain hardening ability.

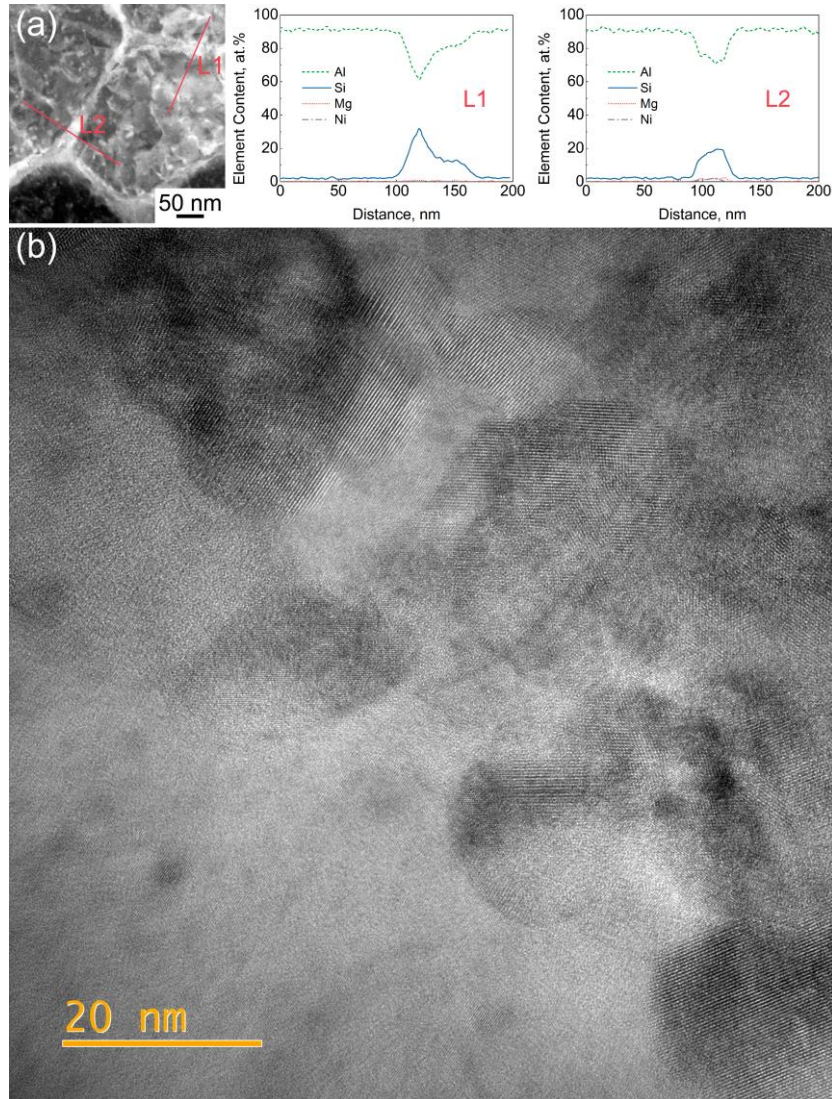


Fig. 6 Details of microstructures parallel to the XY plane: (a) STEM high-angle annular dark-field microstructure along with line scanning analysis of elements; (b) HRTEM microstructure of eutectic boundary.

3.2 Evolution of texture

The high thermal gradient during the LPBF process causes directional solidification, which results in a crystallographic texture (Aboulkhair et al., 2019). Fig. 7 shows the $\varphi_2=0^\circ$ and $\varphi_2=45^\circ$ sections of the determined ODFs of S2 at different strain values. The reference coordinate system TD_t - LD_t - ND_t for texture interpolation is shown in Fig. 7. Here, LD_t of S2 is parallel to LD of S1 in Fig. 2. However, the angle between the incident X-ray beam and the LPBF printing direction of S1 is unavailable. Hence, the angle between TD_t of S2 and TD of S1, or between ND_t of S2 and ND of S1 is unknown. Two main texture components can be observed at the initial state, which include a $\langle 001 \rangle // ND_t$ θ -fiber component and a $\{001\} \langle 110 \rangle$

H shear component (Sidor et al., 2011). As shown, the maximum intensity of the θ -fiber component is only ~ 3.0 multiples of a random density (MRD), and that of the H shear component is only 3.4 MRD. Hence, the texture components are weak (Sidor et al., 2011). In the alloys produced by large plastic deformation, the intensities of texture components can easily exceed 15 MRD. For instance, the maximum intensities of β -fiber and S texture components in a cold-rolled 6016Al alloy are higher than 16 MRD (Sidor et al., 2011). The maximum texture intensity is higher than 18 MRD in a hot-rolled 1050Al alloy (Alvi et al., 2008). Accordingly, the texture in the LPBF AlSi10Mg only presents a weak contribution to the mechanical anisotropy.

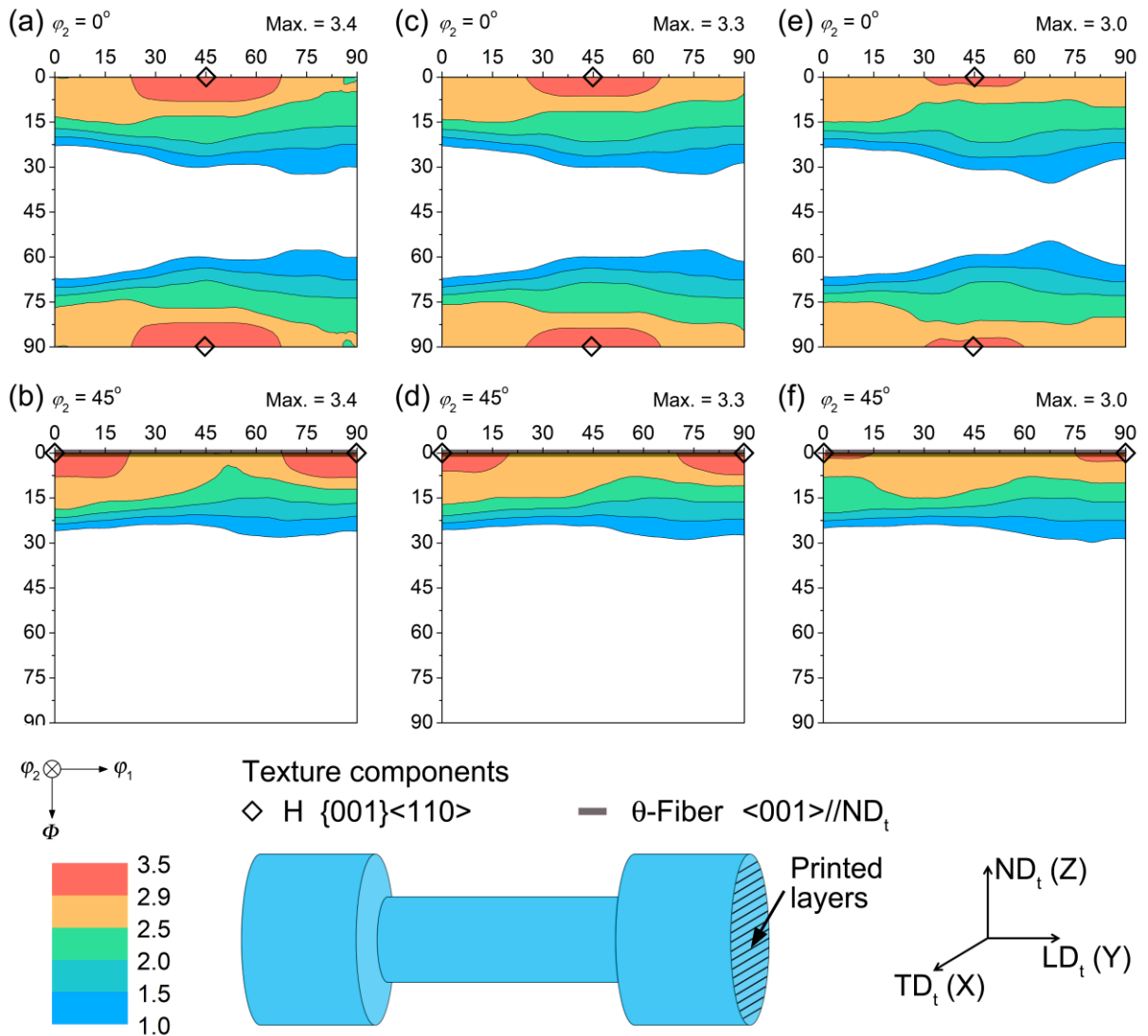


Fig. 7 Texture at the initial state with (a) $\varphi_2=0^\circ$ and (b) $\varphi_2=45^\circ$; at the applied strain of 2.7% with (c) $\varphi_2=0^\circ$ and (d) $\varphi_2=45^\circ$; at the applied strain of 6.6% with (e) $\varphi_2=0^\circ$ and (f) $\varphi_2=45^\circ$.

In the LPBF process, the moving heat source leads to an elongated melt pool (“half-egg” shaped). For the FCC metals, the $\langle 001 \rangle$ direction is the fastest solidification direction. During solidification, the $\langle 001 \rangle$ growing direction and Al dendrite arms are parallel to the temperature gradient vector (perpendicular to the curved melt pool boundary) (Liu and To, 2017), resulting in the θ -fiber and H shear texture components (Takata et al., 2017; Thijs et al., 2013). During plastic deformation, a sufficient dislocation slip activity causes changes in the grain orientations, leading to variations in the texture of the Al matrix. The maximum intensity of the H shear component reduces slightly to 3.3 MRD at the applied strain of 2.7%, and further to 3.0 at the applied strain of 6.6% (Fig. 7).

3.3 Evolution of crystallographic orientation-dependent strains

Fig. 8 shows the LD and TD lattice strains of the selected lattice planes in both phases. The deformation process can be divided into four regions, i.e. region 1, 2, 3, and 4, according to the features of lattice strains, especially the Al LD lattice strains. In Fig. 8(a), these four regions are also marked in the true stress-strain curve of S1.

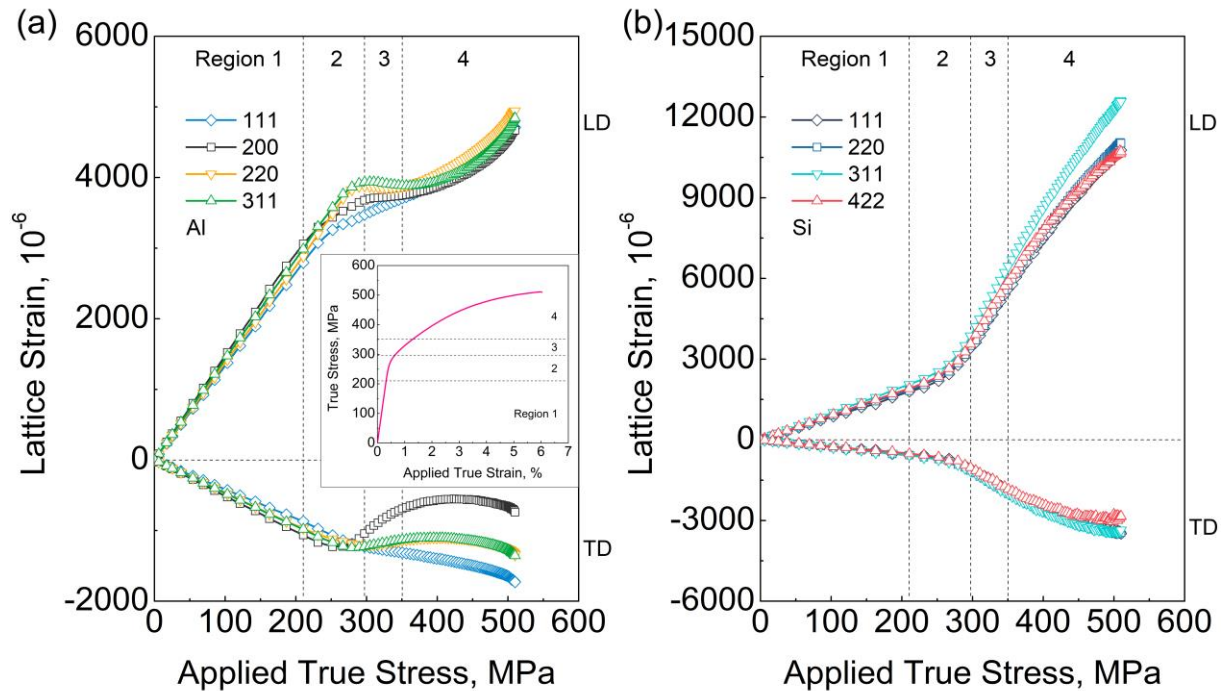


Fig. 8 Measured crystallographic orientation-dependent strains of the selected lattice planes in the (a) Al and (b) Si phases. The inserted graph in (a) shows the four regions in the true stress-strain curve of S1.

(1) Region 1: Elastic deformation

With the applied true stress from 0 to 210 MPa, an initial linear region (region 1) in the lattice strain curves denotes the elastic deformation stage (Fig. 8). Different slopes of the lattice strain vs. applied true stress curves reflect the elastic anisotropy. It is found that the {111} DEM is the highest in both phases, and the {200} DEM is the lowest in the Al phase, in accord with previous investigations (Erdely et al., 2018; Harjo et al., 2017b). Furthermore, the predicted {*hkl*} DEM and Poisson's ratio from the ISODEC software (Gnaeupel-Herold, 2012) based on the Kröner model (Kröner, 1958) are summarized in Table 4. It can be seen that the measured values of the normalized DEM agree well with the predictions for both Al and Si phases.

(2) Region 2: Micro elastoplastic transition I

The applied true stress range from 210 to 297 MPa can be defined as region 2, i.e. micro elastoplastic transition I (mEPT I). In this region, the $\varepsilon_{111}^{\text{ALLD}}$ and $\varepsilon_{200}^{\text{ALLD}}$ curves bend downward, while the $\varepsilon_{220}^{\text{AL,LD}}$ and $\varepsilon_{311}^{\text{AL,LD}}$ curves show upward inflections (Fig. 8(a)). These results reveal that local plastic deformation starts to initiate in some grain families (e.g. Al {111} and {200}), while other grain families (e.g. Al {220} and {311}) remain elastic. Such a deformation incompatibility leads to load transfer from the yielded grain families to the unyielded ones. Besides, load transfer from the Al matrix to the Si particles also increases. In other words, the intergranular and interphase strains and stresses arise.

(3) Region 3: micro elastoplastic transition II

Region 3 at the applied true stress range from 297 to 351 MPa can be defined as mEPT II. Fig. 8(a) shows that the Al {111}, {200}, {220}, and {311} grain families yield at the applied true stresses of 242, 223, 280, and 279 MPa, respectively. The yielding sequence of the selected Al grain families is {200} \rightarrow {111} \rightarrow {311} \rightarrow {220}. The yield strength of each grain family depends on the Taylor factor. A higher Taylor factor value corresponds to higher yield strength. The present experiment implies that the sequence of the Taylor factor values is {200} < {111} < {311} < {220}. Several models can predict the Taylor factor. For FCC metals, the Taylor factor value of the {200}, {220} and {111} grain families predicted by the Taylor upper-bound model are 2.449, 3.674, and 3.674, respectively (Clausen et al., 1998). They are 2.449, 2.449, and 3.674, respectively, as predicted by the Sachs lower-bound model or Hutchinson elastic-plastic self-consistent model (Clausen et al., 1998). It can be seen that the Taylor model is closer to the present experimental results. Note that all these models neglect the direct interactions between grains, which have a significant impact on the elastoplastic deformation.

After yielding, the Al {220} and {311} curves show lattice strain plateaus, the Al {200}

curve rises slightly, and the Al {111} curve rises linearly with a more pronounced slope (Fig. 8(a)). Those differences should be associated with different numbers of activated slip systems in various grain families, which are further dependent on the crystallographic orientation (Diehl, 1956), as well as the interactions between the adjacent grains (Bieler et al., 2019). These differences also indicate that the local strain hardening behavior varies in different $\{hkl\}$ grain families, which will be further discussed in section 3.7.

As the deformation proceeds, the differences between the $\{hkl\}$ lattice strains in the LD decrease in this region, indicating the reductions in the intergranular strains in the LD. In contrast, the intergranular strains in the TD increase (Fig. 8(a)). In this region, sufficient plastic slip activity occurs in the Al matrix, leading to a significant load transfer from the Al matrix to the Si precipitates. Fig. 8(b) shows that the lattice strains in the Si phase in the LD increase rapidly from the level of $\sim 3700 \times 10^{-6}$ to $\sim 6000 \times 10^{-6}$.

(4) Region 4: Plastic deformation with continuous hardening

After the mEPT II stage, multiple slip systems are activated in different Al grain families, leading to a continuous hardening. This plastic deformation stage can be defined as region 4. In this region, the Al lattice strains increase when the plastic deformation proceeds (Fig. 8(a)). It can be seen that the average differences between various Al lattice strains in the TD become more significant than those in region 3, indicating further developments of intergranular strains in the TD in the Al matrix. As a result of increased load transfer, the lattice strains of Si in the LD increase continuously and rapidly (Fig. 8(b)).

In sum, as plastic deformation occurs in the Al matrix, the $\varepsilon_{hkl}^{Al,LD}$ vs. applied true stress curves of Al bend downward, while the $\varepsilon_{hkl}^{Si,LD}$ vs. applied true stress curves of Si show upward inflections (Fig. 8), indicating an increased load transfer effect. Meanwhile, the intergranular strains within the Al matrix in region 4 decrease in the LD and increase in the TD, compared with those in region 3.

3.4 Evolution of average phase strains and stresses

The average phase strains obtained from Rietveld refinement are shown in Fig. 9. The maximum average strains in the LD are 4748×10^{-6} and 11221×10^{-6} in the Al and Si phases, respectively. The {311} lattice strains are shown here again for comparison. The {311} lattice strains that are insensitive to the intergranular strains in the face-centered cubic metals are close to the average phase strains (Clausen et al., 1998). The predicted Poisson's ratios of the Al and Si phases are 0.346 and 0.223, respectively. However, these measured ν_{Al} and ν_{Si} values

using Eq. (5) are 0.331 and 0.361, respectively. The measured Poisson's ratio of Al is slightly lower than the prediction, whereas the measured Poisson's ratio of Si is significantly higher than the prediction. This inconsistency is caused by the interphase load transfer effect. Eq. (5) relies on the assumption $\sigma_{i,TD} = \sigma_{i,ND} = 0$, which is not appropriate for multiphase materials. During the uniaxial tensile deformation of the AlSi10Mg alloy, the Al matrix contracts in the TD or ND more than the Si precipitates due to a higher Poisson's ratio of Al. Thus, the Al matrix imposes additionally compressive deformation to the Si precipitates, which in turn impose additionally tensile deformation to the Al matrix. As a result, the measured Al Poisson's ratio is underestimated, and that of Si is overestimated.

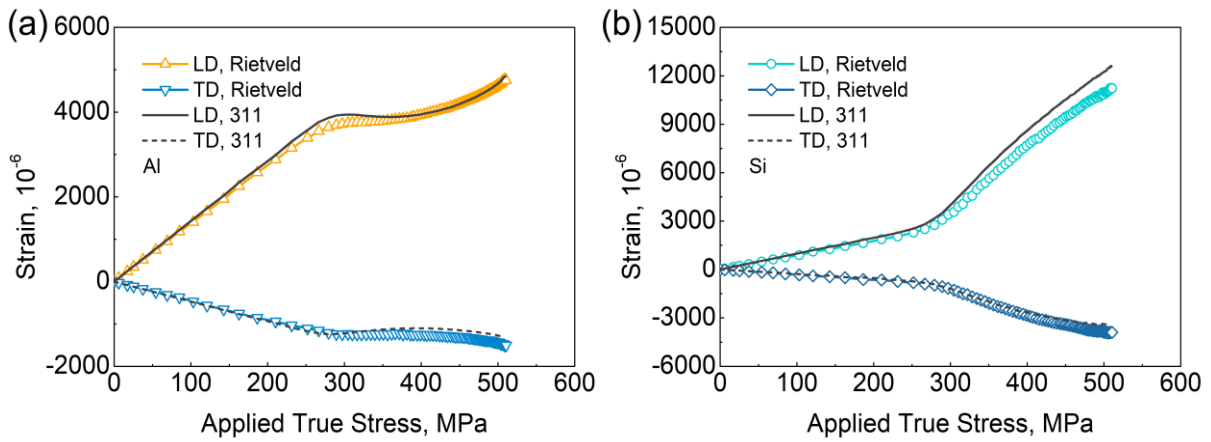


Fig. 9 Average phase strains in the (a) Al and (b) Si phases, which were obtained based on Rietveld refinement. The {311} lattice strains from Fig. 8 are shown here again for comparison.

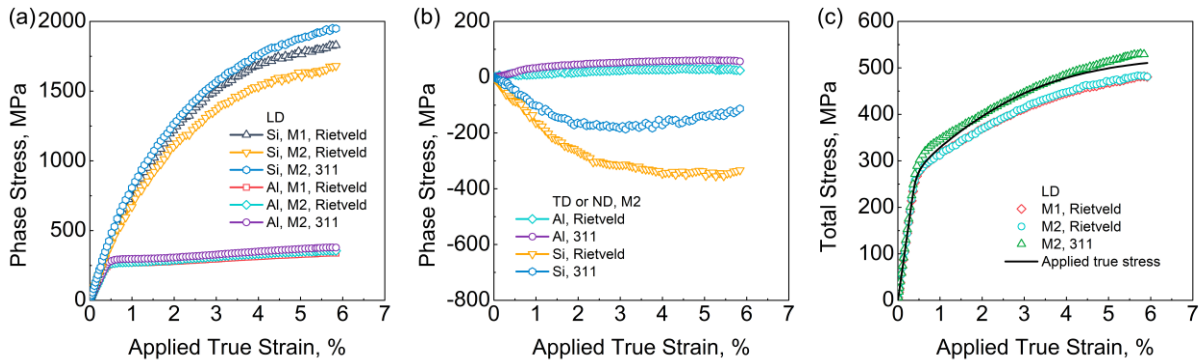


Fig. 10 Comparison of stresses in the LPBF AlSi10Mg alloy determined using different methods: (a) average phase stresses in the LD; (b) average phase stresses in the TD or ND; (c) total LD stresses of the alloy.

The average phase stresses of Al and Si are then calculated using M1 and M2. Fig. 10(a) compares the average phase stresses in the LD of Al and Si, respectively. For the Al average

phase stress in the LD determined from Rietveld strains, the average relative difference between M1 and M2 is 4.3%. This value is 10.0% for the Si phase. The average phase stresses calculated from the $\{311\}$ strains using M2 are also shown here for comparison. The maximum Al average phase stresses in the LD determined from $\{311\}$ strains, and Rietveld strains using M1 and M2 are about 379, 339, and 357 MPa, respectively. The corresponding values for the Si phase are about 1951, 1830, and 1681 MPa, respectively (Fig. 10(a)). It is clear that the Si phase is a strengthening phase.

The average phase stresses in the TD or ND of Al and Si calculated from the Rietveld and $\{311\}$ strains using M2 are shown in Fig. 10(b). The average phase stresses in the TD or ND of Al and Si are tensile and compressive, respectively. Based on the Rietveld strains, the maximum and minimum values in the Al and Si phases are about 31 and -354 MPa, respectively. Based on the $\{311\}$ strains, the corresponding values are 61 and -187 MPa, respectively.

From the determined average phase stresses, the total stress σ_{LD}^{total} in the LD of the alloy may be calculated using (Harjo et al., 2017b)

$$\sigma_{LD}^{total} = f_{Al}\sigma_{Al,LD} + f_{Si}\sigma_{Si,LD}, \quad (16)$$

where f_{Al} and f_{Si} are the volume fractions of Al and Si, respectively. Fig. 10(c) compares the applied stress and the calculated total stresses in the LD. The total stress in the LD calculated from the $\{311\}$ strains shows the best agreement with the applied stress (Fig. 10(c)), with an average relative error of 3.5% during the entire deformation. In contrast, the calculated total stresses in the LD from Rietveld strains using M1 and M2 are virtually coincident. During the elastic stage and early plastic stage, the calculated total stresses agree with the applied stress very well. As the plastic deformation proceeds, the deviation increases. The average relative errors between the calculated total stresses in the LD from M1 and M2 and the applied stress are both 5.3%. Based on the calculated phase stresses from M2 using $\{311\}$ strains, the stress partitioning ratio of Si $f_{Si}\sigma_{Si,LD}/\sigma_{LD}^{total}$ is only about 13.5% during the elastic stage. Then, this $f_{Si}\sigma_{Si,LD}/\sigma_{LD}^{total}$ ratio grows dramatically during the plastic stage until 35.4%. This fact reveals that the strong load-transfer effect of Si makes a significant contribution to the apparent (or macro) strain hardening behavior of the alloy.

It should be mentioned that the Rietveld refinement analysis is known to provide average results of the various $\{hkl\}$ responses, free from elastic or plastic anisotropic effects (Daymond et al., 1997; Steuwer et al., 2010). Hence, the Rietveld strains and stresses are usually viewed as the average phase strains and stresses. Since multiple diffraction peaks are used, the Rietveld

refinement analysis is also insensitive to the intensities of diffraction peaks compared with individual peak fitting (Daymond et al., 1997). This is especially useful for the alloys containing constituent phases with small contents. However, during plastic deformation, the development of intergranular strains can affect the accuracy of the Rietveld refinement analysis slightly.

Residual strains and stresses should be present after the LPBF process because the Al and Si phases have very different thermal and mechanical properties, such as the coefficient of thermal expansion and elastic properties. These residual stresses will superimpose on the stresses caused by the applied load. However, since the reference parameters were measured and refined from the unloading state, the same residual strains and stresses appear in both unloading and loading states and cancel out (Hutchings et al., 2005). Therefore, the measured average phase stresses of Al and Si are those stresses purely caused by the applied load, and they do not include the contributions from the residual stresses caused by the LPBF process.

3.5 Uncertainties of measurements

In the present investigation, the $\theta_{hkl,0}^{i,s}$ (or $a_0^{i,s}$) values were refined using the condition of $\varepsilon_{hkl}^{i,s} = 0$ (or $\varepsilon_{i,s} = 0$) at the unloading state due to the common instabilities at the beginning of the tensile deformation below about 80 MPa (Erdely et al., 2018; Zhong et al., 2015b). The refinement has no influence on the levels of strains, elastic moduli, and final stresses (Erdely et al., 2018; Korsunsky et al., 1998). The $\{hkl\}$ lattice strain uncertainty of phase i in the direction s before d0 refinement, $u_{\varepsilon,hkl}^{i,s}$, is calculated by (Wimpory et al., 2009)

$$u_{\varepsilon,hkl}^{i,s} = \left[\left(\frac{\cos \theta_{hkl,0}^{i,s}}{\sin \theta_{hkl}^{i,s}} \delta \theta_{hkl,0}^{i,s} \right)^2 + \left(\frac{\cos \theta_{hkl}^{i,s} \sin \theta_{hkl,0}^{i,s}}{\sin^2 \theta_{hkl}^{i,s}} \delta \theta_{hkl}^{i,s} \right)^2 \right]^{1/2}, \quad (17)$$

$$\approx \frac{1}{\tan \theta_{hkl,0}^{i,s}} \left[(\delta \theta_{hkl,0}^{i,s})^2 + (\delta \theta_{hkl}^{i,s})^2 \right]^{1/2}$$

where $\delta \theta_{hkl,0}^{i,s}$ and $\delta \theta_{hkl}^{i,s}$ are the fitting uncertainties of $\theta_{hkl,0}^{i,s}$ and $\theta_{hkl}^{i,s}$, respectively. Table 5 summarizes the maximum lattice strain uncertainties before d0 refinement.

The Rietveld strain uncertainty of phase i in the direction s before d0 refinement, $u_{\varepsilon}^{i,s}$, is calculated by (Wimpory et al., 2009)

$$u_{\varepsilon}^{i,s} = \left[\left(\frac{\delta a^{i,s}}{a_0^{i,s}} \right)^2 + \left(\frac{a \delta a_0^{i,s}}{(a_0^{i,s})^2} \right)^2 \right]^{1/2} \approx \frac{1}{a_0^{i,s}} \left[(\delta a^{i,s})^2 + (\delta a_0^{i,s})^2 \right]^{1/2}. \quad (18)$$

Here, $\delta a^{i,s}$ and $\delta a_0^{i,s}$ are the fitting uncertainties of $a^{i,s}$ and $a_0^{i,s}$, respectively. Using Eq. (18), the determined maximum Rietveld strain uncertainties in the LD and TD of Al are 19.01

$\times 10^{-6}$ and 28.93×10^{-6} , respectively, during the entire loading. These two values of Si are 408.88×10^{-6} and 482.39×10^{-6} , respectively. The results indicate that the Rietveld strain uncertainties are comparable to the $\{hkl\}$ lattice strain uncertainties.

The stress uncertainty of phase i in the LD before d0 refinement, $u_{\sigma}^{i,LD}$, is calculated by (Wimpory et al., 2009)

$$u_{\sigma}^{i,LD} = \left[\left(\frac{E_i}{1+\nu_i} u_{\varepsilon}^{i,LD} \right)^2 + \left(\frac{\nu_i E_i}{(1+\nu_i)(1-2\nu_i)} \right)^2 \left((u_{\varepsilon}^{i,LD})^2 + (u_{\varepsilon}^{i,TD})^2 + (u_{\varepsilon}^{i,ND})^2 \right) \right]^{1/2}, \quad (19)$$

where $u_{\varepsilon}^{i,LD}$, $u_{\varepsilon}^{i,TD}$, and $u_{\varepsilon}^{i,ND}$ are the strain uncertainties in the LD, TD, and ND, respectively. Here, $u_{\varepsilon}^{i,ND} = u_{\varepsilon}^{i,TD}$ based on the assumption of M2. Using the Rietveld strain uncertainties, the determined maximum stress uncertainties in the LD of Al and Si are about 2.9 and 69.1 MPa, respectively, during the entire loading. In contrast, using the $\{311\}$ lattice strain uncertainties, the calculated maximum stress uncertainties in the LD of Al and Si are about 2.0 and 48.7 MPa, respectively. Note that the exact determination of the propagated uncertainties in the lattice strains and phase stresses cannot be achieved (Erdely et al., 2018). Nevertheless, the refinement should only have a weak effect on the final strain and stress uncertainties (Erdely et al., 2018; Korsunsky et al., 1998).

3.6 Load transfer in the LPBF AlSi10Mg and conventional Al-Si-x alloys

The LPBF AlSi10Mg alloy has a very different microstructure and micromechanical properties compared with the conventional Al-Si- x ($x = \text{Mg, Cu, or other elements}$) alloys. For instance, the cast AlSi10Mg alloy is characterized by large Al dendrites (typically larger than $50 \mu\text{m}$) and irregular coarse eutectic network (Girelli et al., 2019; Schöbel et al., 2014). Meanwhile, the Si particles have large sizes, e.g. about $5.7 \mu\text{m}$ in a cast A356 alloy (Dighe and Gokhale, 1997) and about $20 \mu\text{m}$ in a cast AlSi17Cu4 alloy (Schöbel et al., 2014). The coarse eutectic network and Si particles have weak constraints to the Al matrix during deformation. Besides, they are much easier to fracture (DelRio et al., 2015).

The fracture strength of Si particles tends to decrease with increasing their sizes because of the increased defect density in larger-sized Si particles (DelRio et al., 2015). Therefore, the large-sized Si particles in conventional Al-Si- x alloys can only bear small strains and stresses. For instance, Davidson et al. (Davidson et al., 2017) measured the Al and Si average phase stresses in an A356 alloy manufactured from sand casting and hot-isostatic pressing using in-situ neutron diffraction. They showed that the maximum principle lattice strain and stress in the

Si particles are only $\sim 2700 \times 10^{-6}$ and ~ 400 MPa, respectively, when the alloy was subjected to tensile deformation. These two values are about 24% and 21% of the corresponding ones in the present study. Schöbel et al. (Schöbel et al., 2014) measured the Al and Si lattice strains in the cast AlSi7MgCu and AlSi17Cu4 alloys during tensile deformation at different temperatures using in-situ neutron diffraction. At room temperature, the maximum Si lattice strains in AlSi7MgCu and AlSi17Cu4 are $\sim 3150 \times 10^{-6}$ and $\sim 2150 \times 10^{-6}$, respectively, which are about 28% and 19% of those in the present study. The maximum Si phase strain in the LD of another LPBF AlSi10Mg alloy is about 12000×10^{-6} , as measured by Kim et al. (Kim et al., 2017) using in-situ neutron diffraction, which is close to the present result. Therefore, it can be concluded that the nano-sized Si particles in the LPBF AlSi10Mg are much stronger. They are able to bear much higher stress and fracture much later. This is an important factor why the mechanical properties of the LPBF AlSi10Mg alloy are superior to those of the cast counterpart.

3.7 Strain hardening behavior of the Al matrix

The Si particles in the present LPBF AlSi10Mg are nano-sized and mainly distributed in the eutectic cell boundary network. These Si particles not only introduce significant Orowan strengthening and load transfer effect but also have a substantial impact on the strain hardening behavior due to their strong interactions with dislocations. Hence, it is essential to analyze the strain hardening behavior at the microscale.

In order to obtain the hardening coefficients of different grain families at the microscale, the total strain of Al $\varepsilon_{\text{Al,LD}}^{\text{total}}$ is required. Although the Si phase may experience twinning deformation in the LPBF AlSi10Mg during deformation (Kim et al., 2017), its total strain should approximate its elastic strain and should be very small. Therefore, it is assumed that the total strain of Al $\varepsilon_{\text{Al,LD}}^{\text{total}}$ equals the applied total strain. The stresses in the LD of different grain families $\sigma_{hkl}^{\text{Al,LD}}$ are also required, which can be calculated by (Withers and Bhadeshia, 2001)

$$\sigma_{hkl}^{\text{Al,LD}} = A_{hkl}^{\text{Al}} \left(B_{hkl}^{\text{Al}} \varepsilon_{hkl}^{\text{Al,LD}} + 2\nu_{hkl}^{\text{Al}} \varepsilon_{hkl}^{\text{Al,TD}} \right), \quad (20)$$

where $A_{hkl}^{\text{Al}} = E_{hkl}^{\text{Al}} \left[\left(1 + \nu_{hkl}^{\text{Al}} \right) \left(1 - 2\nu_{hkl}^{\text{Al}} \right) \right]^{-1}$, $B_{hkl}^{\text{Al}} = 1 - \nu_{hkl}^{\text{Al}}$. The values of E_{hkl}^{Al} and ν_{hkl}^{Al} are shown in Table 4. Then the hardening coefficients of different grain families at the microscale can be estimated approximately.

The evolutions of $\sigma_{111}^{\text{Al,LD}}$, $\sigma_{311}^{\text{Al,LD}}$ and $\sigma_{\text{Al,LD}}$ with $\varepsilon_{\text{Al,LD}}^{\text{total}}$ are shown in Fig. 11(a). The corresponding evolutions of the microscopic hardening coefficients ($d\sigma_{111}^{\text{Al,LD}}/d\varepsilon_{\text{Al,LD}}^{\text{total}}$, $d\sigma_{311}^{\text{Al,LD}}/d\varepsilon_{\text{Al,LD}}^{\text{total}}$, and $d\sigma_{\text{Al,LD}}/d\varepsilon_{\text{Al,LD}}^{\text{total}}$) with stress are shown in Figs. 11(b) and (c). The microscopic Kocks–Mecking plot in Fig. 11(b) indicates that the strain hardening behavior of

the Al {111} grain family includes EPT stage and stage III (Kocks and Mecking, 2003). In contrast, the strain hardening behavior of the Al {311} grain family includes stages I, II, and III (Kocks and Mecking, 2003). Fig. 11(c) shows the average strain hardening behavior of the Al matrix, which represents the average behavior of all $\{hkl\}$ grain families and can be divided into stages A, B, and C. The crystallographic orientation-dependent strain hardening behavior is related to the number of active slip systems (Diehl, 1956; Takeuchi, 1975; Ungar et al., 2014).

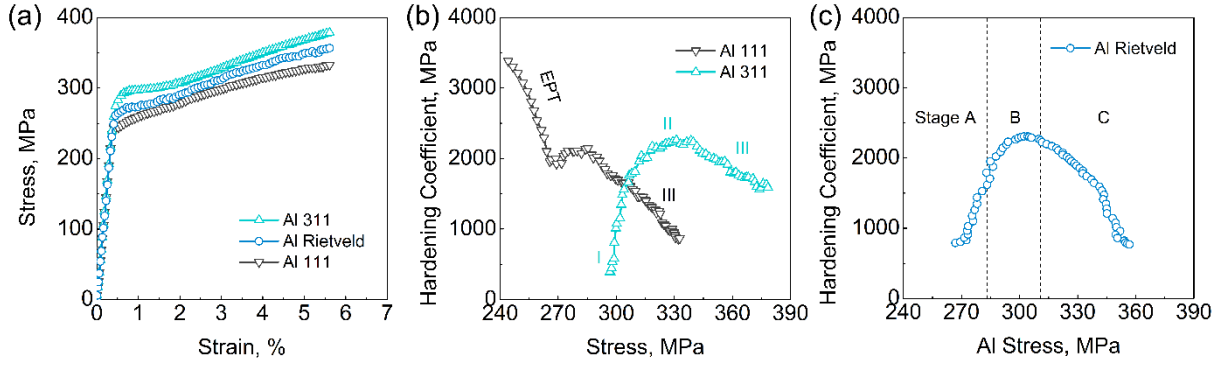


Fig. 11 Mechanical properties of the Al matrix: (a) Al {111}, {311} and average stress-strain curves; (b) $\{hkl\}$ hardening coefficient $d\sigma_{hkl}^{Al,LD}/d\varepsilon_{Al,LD}^{total}$ of Al vs. stress $\sigma_{hkl}^{Al,LD}$; (c) average hardening coefficient $d\sigma_{Al,LD}/d\varepsilon_{Al,LD}^{total}$ of Al vs. stress $\sigma_{Al,LD}$.

It should be mentioned that the total strains of the Al {111} and {311} grain families are assumed to be the same as the applied total strain in the above discussion. In reality, because of elastic and plastic anisotropies, the total strains of the Al {111} and {311} grain families should be different slightly. Nevertheless, this assumption should not change the basic characteristics of $d\sigma_{111}^{Al,LD}/d\varepsilon_{Al,LD}^{total}$ and $d\sigma_{311}^{Al,LD}/d\varepsilon_{Al,LD}^{total}$. In other words, the presence of EPT stage and stage III in the Al {111} grain family should be doubtless, as well as the existence of stages I, II, and III in the Al {311} grain family. Additional supports for this conclusion can be found in Fig. 8, where the Al {111} lattice strain increases continuously in region 3, and the Al {311} lattice strain in the LD is almost flat in region 3.

Further analysis of the strain hardening behavior demands the knowledge of dislocation density, which is associated with broadening of the diffraction profiles. The evolutions of the raw FWHM (in the 2θ space) of Al and Si are shown in Figs. 12(a) and (b). The uncertainties of the raw FWHM are also shown. With the applied true strain increasing to 0.35% (i.e. in the macroscopic elastic stage), the Al $\{hkl\}$ FWHM decreases slightly (Fig. 12(a)). This reduction should be attributed to weak dislocation annihilation, which has also been found in the literature (Zhang et al., 2020; Zhong et al., 2015a). When plastic deformation occurs, the Al $\{hkl\}$ FWHM

increases quickly, indicating an increased dislocation density. After the applied true strain of $\sim 1\%$, the increasing rate of Al $\{hkl\}$ FWHM decreases. They are almost proportional to the applied true strain (Fig. 12(a)). The variation in the growing tendency of Al $\{hkl\}$ FWHM implies a change in the dislocation activity, which will be discussed in the following.

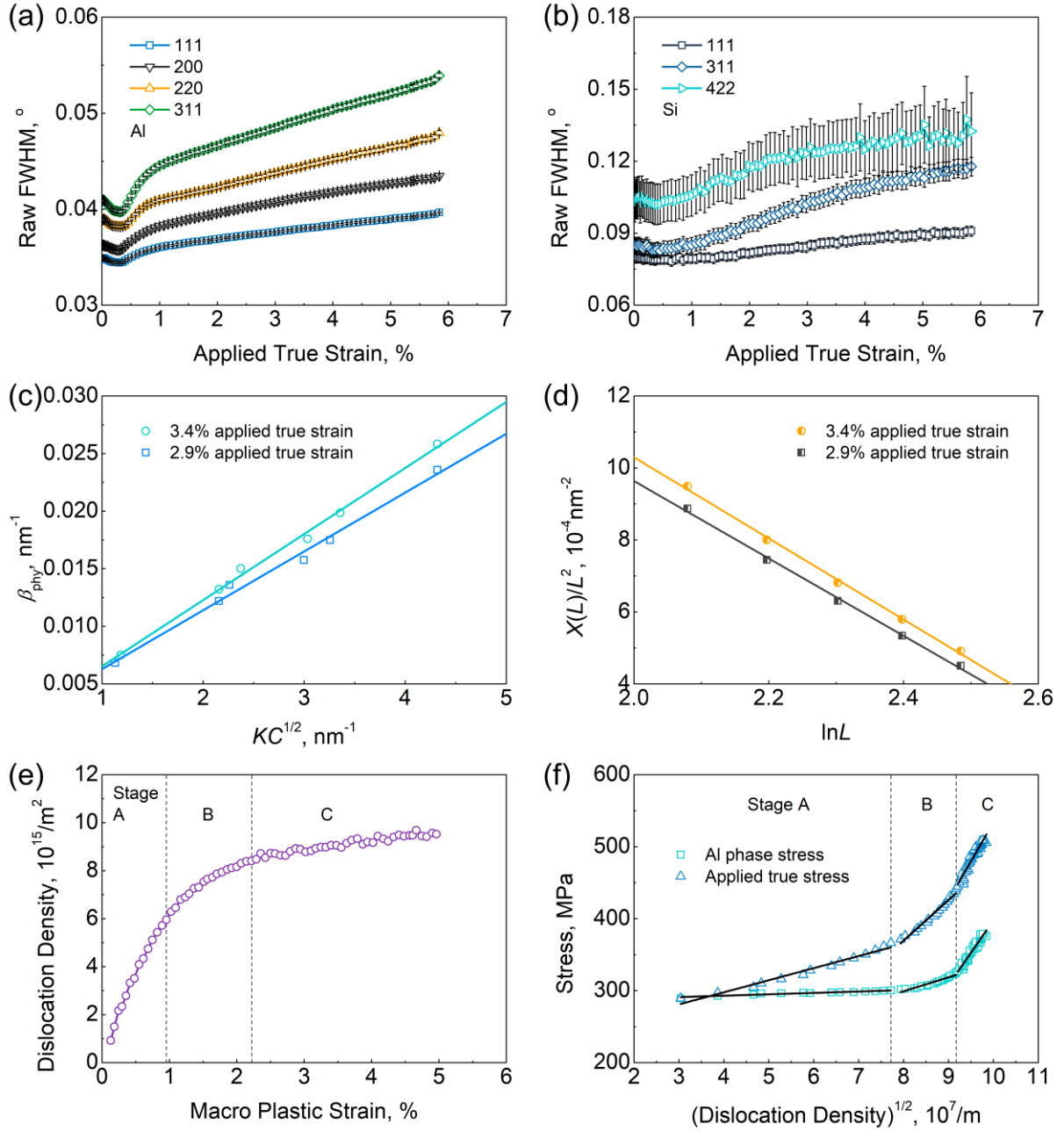


Fig. 12 For dislocation density: the raw FWHM of the (a) Al and (b) Si phases; (c) the mWH plot; (d) linear fitting between $X(L)/L^2$ and $\ln L$; (e) ρ in the Al matrix vs. macro plastic strain; and (f) the Al average phase stress and applied true stress vs. $\sqrt{\rho}$ in the Al matrix. The lines in (f) denote piecewise linear regressions.

The Si $\{hkl\}$ FWHM is almost constant in the elastic stage; afterward, it increases visibly (Fig. 12(b)). The increase in Si $\{hkl\}$ FWHM may be associated with two potential reasons. On the one hand, Kim et al. (Kim et al., 2017) have found out that the stacking faults and twins form in the Si particles due to stress concentrations. Accordingly, the Si $\{hkl\}$ FWHM could increase (Ungar et al., 1998). On the other hand, the stress in the Si particles is not homogeneous (Kim et al., 2017). This heterogeneity could also increase FWHM.

The dislocation density in the Al matrix is analyzed using both the mWH and mWA methods (Arechabaleta et al., 2016; Sahu et al., 2012; Ungar et al., 1998). The mWH plot is shown in Fig. 12(c), and the linear fitting of $X(L)/L^2$ vs. $\ln L$ for the mWA analysis is shown in Fig. 12(d). The results for the applied true strains of 2.9% and 3.4% are demonstrated. Fig. 12(c) shows that the slope of the $\beta_{\text{phy}} - KC^{1/2}$ line increases with increasing the applied true strain, confirming an increased dislocation density. Fig. 12(d) shows that the magnitude of the slope of the $X(L)/L^2$ vs. $\ln L$ line increases with increasing the applied true strain, which also validates an increase in the dislocation density. The determined dislocation density of the Al matrix is shown in Fig. 12 (e), where the stages A, B, and C are marked. At the macroscopic yield strength of the alloy, the dislocation density is $9.2 \times 10^{14} \text{ m}^{-2}$. It increases quickly to $6.0 \times 10^{15} \text{ m}^{-2}$ at 0.95% macro plastic strain (end of stage A), then to $8.4 \times 10^{15} \text{ m}^{-2}$ at 2.2% macro plastic strain (end of stage B), and finally to $9.5 \times 10^{15} \text{ m}^{-2}$ at 5.0% macro plastic strain (Fig. 12 (e)).

The strain hardening due to the dislocations follows the Taylor equation (Taylor, 1934)

$$\sigma = \sigma_0 + \bar{M} \alpha \mu b \sqrt{\rho}, \quad (21)$$

where σ is the mechanical strength of the obstacles to dislocation glide, σ_0 the friction stress, \bar{M} the average Taylor factor, α the strengthening coefficient, and μ the shear modulus. Typically, the linear relationship between the flow stress and $\sqrt{\rho}$ is simplex for polycrystalline metals, i.e. only a single α value exists (Kocks and Mecking, 2003). This has been widely investigated in various materials (He et al., 2018; Liang et al., 2015; Zhong et al., 2015a; Zhou et al., 2016). However, Fig. 12 (f) indicates that the relationship between the Al average phase stress and $\sqrt{\rho}$ is a nonlinear function. Here, the Al average phase stress calculated from Al $\{311\}$ strains using M2 is taken to represent σ . For the Al alloys, $\bar{M} = 3.06$ (Roters et al., 2000; Zhong et al., 2015a), $\mu = 26.4 \text{ GPa}$, and $b = 0.286 \text{ nm}$. Therefore, the α values estimated from the piecewise linear regression in Fig. 12 (f) are 0.0084, 0.084, and 0.39 for stages A, B, and C, respectively. The α value in stage C is within the typical

range of the FCC metals (Mughrabi, 2016; Sauzay and Kubin, 2011), while the α values are quite small in stages A and B.

The applied true stress is also a piecewise linear function of $\sqrt{\rho}$ (Fig. 12 (f)). The determined pseudo- α values based on the applied true stress for stages A, B, and C are 0.073, 0.24, and 0.47, respectively, which are far away from the determined values based on the Al average phase stress. Since the applied true stress contains a large stress contribution from the Si phase, it is not appropriate to calculate the physical α values for the Al phase using the applied true stress. From these results, it is evident that the investigation of the load partitioning between phases is critical to determine the accurate values of the strengthening coefficient α .

Several investigations have also shown that the α values of some steels change during plastic deformation (Bahl et al., 2017; Harjo et al., 2017a; Ungar et al., 2017; Ungar et al., 2014). For instance, Ungar et al. (Ungar et al., 2014) have found out that the α value of the AISI-316 stainless steel depends on the crystallographic-orientation, which should be associated with heterogeneous dislocation arrangements (Feaugas, 1999; Ungar et al., 2014).

In the present work, the grain boundaries, eutectic cell boundaries, and Si/Al interfaces of the LPBF AlSi10Mg alloy provide sources for dislocation nucleation. During plastic deformation, a large number of dislocations are generated from these sites, especially near the stress concentrations. According to the Orowan equation, the shear plastic strain γ can be expressed as (Orowan, 1940)

$$\gamma = \rho_m b \bar{x}, \quad (22)$$

where ρ_m is the mobile dislocation density, \bar{x} the average distance a dislocation moves. Since the dislocation motions are mainly limited inside cells, the \bar{x} value should be less than or equal to the average cell size. In this regard, the mobile dislocation density has to increase continuously to keep the applied strain. Hence, the combination of a large number of dislocation sources and limited motions of dislocations leads to a high dislocation multiplication rate in stage A (Fig. 12(e)).

Because most dislocations are trapped within cells, the interactions between dislocations from adjacent cells are negligible in stage A, which weakens the mutual interactions of dislocations. Meanwhile, thick dislocation forests are not formed yet. The interaction between mobile dislocations and dislocation forests is also weak. In addition, the Si precipitates within cells have a large inter-precipitate distance (Hadadzadeh et al., 2018b; Xiao et al., 2019). For instance, the distance between the Si precipitates inside cells ranges from about 40 to 200 nm

(Hadadzadeh et al., 2018a; Hadadzadeh et al., 2018b; Kim et al., 2017), which is much larger than the typical inter-precipitate distance in the high-strength Al alloys, e.g. ~ 2 nm in the artificial-aged 7xxx Al alloys (Li et al., 2008; Wang and Ma, 2009). Hence, only a small fraction of dislocations can be pinned by the Si precipitates during early plastic deformation. Because of the above mechanisms, the fraction of mobile dislocations is high, and the forest dislocation density only increases slightly, leading to a weak strain hardening effect in stage A (Hull and Bacon, 2011; Sauzay and Kubin, 2011).

The theoretical value of the Taylor strengthening coefficient α in stage A strain hardening may be estimated from the mutual interactions between parallel dislocations. The maximum interaction shear stress τ_{em} between two parallel edge dislocations moving on one slip system reads (Hull and Bacon, 2011)

$$\tau_{em} = \frac{1}{8\pi(1-\nu_{Al})} \mu b \frac{1}{h}, \quad (23)$$

where h is the average distance between the parallel planes of the slip system. Similarly, the maximum interaction shear stress τ_{sm} between two parallel screw dislocations moving on one slip system is (Hull and Bacon, 2011)

$$\tau_{sm} = \frac{1}{4\pi} \mu b \frac{1}{h}. \quad (24)$$

For a material with a dislocation density ρ , the average dislocation distance is $1/\sqrt{\rho}$ if the dislocations are randomly distributed. During uniaxial tensile deformation, the maximum shear stress appears at the 45° plane. Therefore, the average distance between the parallel planes of the slip system may be calculated by

$$h \simeq \frac{1}{\sqrt{\rho}} \cos 45^\circ = \frac{1}{\sqrt{2}} \frac{1}{\sqrt{\rho}}. \quad (25)$$

Then, Eqs. (23)-(24) becomes

$$\tau_{em} = \frac{1}{8\pi(1-\nu_{Al})} \mu b \frac{1}{h} = \frac{\sqrt{2}}{8\pi(1-\nu_{Al})} \mu b \sqrt{\rho}, \quad (26)$$

$$\tau_{sm} = \frac{1}{4\pi} \mu b \frac{1}{h} = \frac{\sqrt{2}}{4\pi} \mu b \sqrt{\rho}. \quad (27)$$

Eqs. (26)-(27) implies that the maximum α values are 0.086 and 0.11 for edge and screw dislocations, respectively, in stage A strain hardening.

As plastic deformation proceeds, more and more dislocations are accumulated near the

cell boundaries or Si precipitates to form dislocation forests (Li et al., 2020; Wu et al., 2016). As a result, the mutual interactions of dislocations become stronger and stronger. The dislocation forests produce back-stress fields that make the generation of further dislocations more difficult and hinders the dislocation motions. Consequently, the increasing rate of dislocation density reduces in stages B and C (Fig. 12(e)). Moreover, the dislocation forests reduce dislocation mobility, resulting in a strong dislocation strengthening effect in stages B and C, respectively (Fig. 12(f)).

The α values in monotonic, cyclic, and quasi-stationary deformations have also been reviewed by Mughrabi (Mughrabi, 2016). He concluded that the α value is ~ 0.1 for primary slip interaction (plastic deformation with a single slip system) and ~ 0.35 for primary/secondary slip interaction (plastic deformation with multiple slip systems). During steady-state plastic deformation, the α value decreases from ~ 0.35 to ~ 0.25 , which is dominated by the increased heterogeneity of dislocation pattern (Mughrabi, 2016). For the present work, the α value of 0.33 in stage C can be viewed as the steady-state value.

To summarize, the total dislocation density in the Al matrix increases significantly during plastic deformation. A multistage strain hardening phenomenon is observed in the Al matrix, which is related to different dislocation mechanisms in the unique microstructure of the LPBF AlSi10Mg alloy. Those results reveal a quite different deformation mechanism from conventional Al alloys.

4. Conclusions

(1) The hierarchical microstructures and macro mechanical properties of the LPBF AlSi10Mg alloy were examined. The good combination of strength and ductility results from a low porosity, the small-sized grains (Zhang et al., 2021), the nano-sized Si particles introducing Orowan strengthening, the significant load transfer effect, and a good strain hardening ability. The texture shows a weak $\langle 001 \rangle$ fiber component combined with a weak $\{001\} \langle 110 \rangle$ H shear component, which has a weak influence on the mechanical properties of the alloy.

(2) The evolution of crystallographic orientation-dependent lattice strains can be divided into four regions: region 1 (elastic deformation), 2 (micro elastoplastic transition I), 3 (micro elastoplastic transition II), and 4 (plastic deformation with continuous hardening). The measured lattice strains reveal an inhomogeneous deformation at the grain and phase scale. The evolutions of lattice strains in the elastic stage are governed by the elastic properties and microstructure. In contrast, the evolutions of lattice strains in the plastic stage are dominated by

elastic and the plastic anisotropy in the Al matrix, as well as the elastic mismatch and plastic misfit between phases.

(3) The nano-sized Si particles introduce a significant load transfer effect, which is much stronger than the one caused by the Si particles in those Al-Si-*x* alloys produced by conventional methods. The average phase stress of Si reflects the high strength of the nano-sized Si particles. The in-situ measured results indicate that the maximum stress in the present Si particles reaches up to ~2 GPa. The high-strength nano-sized Si particles make an essential contribution to the apparent strain hardening capacity of the alloy because they carry a continuously growing high stress during the plastic deformation. The measurements show that the stress partitioning ratio of Si can reach up to 35.4%, although the volume fraction of Si is only 9.63%.

(4) An unusual strain hardening phenomenon at the microscale is detected. The Al matrix experiences a multistage strain hardening behavior. In stage A, the dislocation density increases quickly but with a weak strain hardening effect. In stages B and C, the dislocation density increases slowly; yet, the strain hardening effect becomes more vigorous. This behavior is associated with the unique microstructure formed during the LPBF process. Since the eutectic cell boundary network imposes strong constraints on the mobile dislocations, most dislocations are trapped in the cells. The mutual interactions between dislocations from adjacent cells are suppressed. The dislocation interactions become strong until the dislocation density within cells is high enough. Then the strain hardening effect turns to be significant.

5. Outlook

Although the mechanical properties of the LPBF AlSi10Mg are superior compared with its cast counterpart, it is still challenging to replace high-performance aluminum components, e.g. high-grade forged parts. Consequently, new AM-specific low-cost aluminum alloys with higher mechanical properties than AlSi10Mg need to be developed without adding rare-earth elements. Furthermore, micromechanical investigations are indispensable in the development and optimization of new AM-specific alloys.

Declaration of competing interest

The authors declare that they have no competing interests.

CRedit authorship contribution statement

X.X. Zhang: Conceptualization, data curation, formal analysis, methodology, investigation, visualization, writing - original draft, writing - review & editing; **A. Lutz:** Data

curation, investigation, writing - review & editing; **H. Andrä:** Project administration, funding acquisition, writing - review & editing; **M. Lahres:** Funding acquisition, writing - review & editing; **W.M. Gan:** Investigation, methodology, writing - review & editing; **E. Maawad:** Investigation, methodology, writing - review & editing; **C. Emmelmann:** Funding acquisition, writing - review & editing.

Acknowledgments

The authors gratefully acknowledge support from the project CustoMat_3D, which was sponsored by the German Federal Ministry of Education and Research (BMBF) with No. 03XP0101I. This work was also supported by the Fraunhofer Cluster of Excellence “Programmable Materials”. The authors are very grateful to Prof. H-G. Brokmeier’s group and the GEMS-P staff at DESY, Hamburg, Germany, for their kind support of the experiments.

List of abbreviations

DEM: diffraction elastic modulus

EDX: energy-dispersive X-ray

EPT: elastoplastic transition

FCC: face-centered cubic

FWHM: full width at half maximum

HRTEM: high-resolution transmission electron microscopy

LD: loading direction

LDt: loading direction for texture measurement

LPBF: laser powder bed fusion

M1: first method of stress calculation

M2: second method of stress calculation

mEPT: micro elastoplastic transition

MRD: multiples of a random density

mWA method: modified Warren-Averbach method

mWH method: modified Williamson-Hall method

ND: normal direction

NDt: normal direction for texture measurement

ODF: orientation distribution function

OM: optical microscopy

PM: powder metallurgy

S1: Specimen 1 for strains, stresses and dislocation density measurements

S2: Specimen 2 for texture measurement

STEM: scanning transmission electron microscopy

SXRD: synchrotron X-ray diffraction

TD: transverse direction

TDt: transverse direction for texture measurement

TEM: transmission electron microscopy

References

MAUD: Materials Analysis Using Diffraction, <http://maud.radiographema.com/>, accessed on June 01, 2019.

Aboulkhair, N.T., Everitt, N.M., Ashcroft, I., Tuck, C., 2014. Reducing porosity in AlSi10Mg parts processed by selective laser melting. *Addit. Manuf.* 1-4, 77-86.

Aboulkhair, N.T., Simonelli, M., Parry, L., Ashcroft, I., Tuck, C., Hague, R., 2019. 3D printing of aluminium alloys: additive manufacturing of aluminium alloys using selective laser melting. *Prog. Mater. Sci.* 106, 100578.

Alvi, M.H., Cheong, S.W., Suni, J.P., Weiland, H., Rollett, A.D., 2008. Cube texture in hot-rolled aluminum alloy 1050 (AA1050) - nucleation and growth behavior. *Acta Mater.* 56, 3098-3108.

Arechabaleta, Z., van Liempt, P., Sietsma, J., 2016. Quantification of dislocation structures from anelastic deformation behaviour. *Acta Mater.* 115, 314-323.

Bahl, S., Suwas, S., Ungar, T., Chatterjee, K., 2017. Elucidating microstructural evolution and strengthening mechanisms in nanocrystalline surface induced by surface mechanical attrition treatment of stainless steel. *Acta Mater.* 122, 138-151.

Bieler, T.R., Alizadeh, R., Peña-Ortega, M., Llorca, J., 2019. An analysis of (the lack of) slip transfer between near-cube oriented grains in pure Al. *Int. J. Plast.* 118, 269-290.

Chen, B., Moon, S.K., Yao, X., Bi, G., Shen, J., Umeda, J., Kondoh, K., 2017. Strength and strain hardening of a selective laser melted AlSi10Mg alloy. *Scr. Mater.* 141, 45-49.

Chen, L.Y., Xu, J.Q., Choi, H., Pozuelo, M., Ma, X., Bhowmick, S., Yang, J.M., Mathaudhu, S., Li, X.C., 2015. Processing and properties of magnesium containing a dense uniform dispersion of nanoparticles. *Nature* 528, 539-543.

Clausen, B., Lorentzen, T., Leffers, T., 1998. Self-consistent modelling of the plastic

deformation of FCC polycrystals and its implications for diffraction measurements of internal stresses. *Acta Mater.* 46, 3087-3098.

Davidson, C.J., Finlayson, T.R., Fitzpatrick, M.E., Griffiths, J.R., Oliver, E.C., Wang, Q.G., 2017. Observations of the stress developed in Si inclusions following plastic flow in the matrix of an Al-Si-Mg alloy. *Philos. Mag.* 97, 1398-1417.

Daymond, M.R., Bourke, M.A.M., VonDreele, R.B., Clausen, B., Lorentzen, T., 1997. Use of Rietveld refinement for elastic macrostrain determination and for evaluation of plastic strain history from diffraction spectra. *J. Appl. Phys.* 82, 1554-1562.

Dekeijser, T.H., Langford, J.I., Mittemeijer, E.J., Vogels, A.B.P., 1982. Use of the Voigt function in a single-line method for the analysis of X-ray-diffraction line broadening. *J. Appl. Crystallogr.* 15, 308-314.

Delahaye, J., Tchuindjang, J.T., Lecomte-Beckers, J., Rigo, O., Habraken, A.M., Mertens, A., 2019. Influence of Si precipitates on fracture mechanisms of AlSi10Mg parts processed by selective laser melting. *Acta Mater.* 175, 160-170.

DelRio, F.W., Cook, R.F., Boyce, B.L., 2015. Fracture strength of micro- and nano-scale silicon components. *Appl. Phys. Rev.* 2, 021303.

Diehl, J., 1956. Zugverformung von Kupfer-Einkristallen. 1. Verfestigungskurven und Oberflächenerscheinungen. *Z. Metallk.* 47, 331-343.

Dighe, M.D., Gokhale, A.M., 1997. Relationship between microstructural extremum and fracture path in a cast Al-Si-Mg alloy. *Scr. Mater.* 37, 1435-1440.

Erdely, P., Staron, P., Maawad, E., Schell, N., Clemens, H., Mayer, S., 2018. Lattice and phase strain evolution during tensile loading of an intermetallic, multi-phase γ -TiAl based alloy. *Acta Mater.* 158, 193-205.

Feaugas, X., 1999. On the origin of the tensile flow stress in the stainless steel AISI 316L at 300 K: Back stress and effective stress. *Acta Mater.* 47, 3617-3632.

Girelli, L., Tocci, M., Gelfi, M., Pola, A., 2019. Study of heat treatment parameters for additively manufactured AlSi10Mg in comparison with corresponding cast alloy. *Mater. Sci. Eng. A* 739, 317-328.

Gnaeupel-Herold, T., 2012. ISODEC: software for calculating diffraction elastic constants. *J. Appl. Crystallogr.* 45, 573-574.

Hadadzadeh, A., Amirkhiz, B.S., Odeshi, A., Mohammadi, M., 2018a. Dynamic loading of direct metal laser sintered AlSi10Mg alloy: Strengthening behavior in different building directions. *Mater. Des.* 159, 201-211.

- Hadadzadeh, A., Baxter, C., Amirkhiz, B.S., Mohammadi, M., 2018b. Strengthening mechanisms in direct metal laser sintered AlSi10Mg: Comparison between virgin and recycled powders. *Addit. Manuf.* 23, 108-120.
- Harjo, S., Kawasaki, T., Tomota, Y., Gong, W., Aizawa, K., Tichy, G., Shi, Z.M., Ungar, T., 2017a. Work hardening, dislocation structure, and load partitioning in lath martensite determined by in situ neutron diffraction line profile analysis. *Metall. Mater. Trans. A* 48A, 4080-4092.
- Harjo, S., Kubota, S., Gong, W., Kawasaki, T., Gao, S., 2020. Neutron diffraction monitoring of ductile cast iron under cyclic tension-compression. *Acta Mater.* 196, 584-594.
- Harjo, S., Tsuchida, N., Abe, J., Gong, W., 2017b. Martensite phase stress and the strengthening mechanism in TRIP steel by neutron diffraction. *Sci. Rep.* 7, 15149.
- He, S.H., He, B.B., Zhu, K.Y., Huang, M.X., 2018. Evolution of dislocation density in bainitic steel: Modeling and experiments. *Acta Mater.* 149, 46-56.
- Herzog, D., Seyda, V., Wycisk, E., Emmelmann, C., 2016. Additive manufacturing of metals. *Acta Mater.* 117, 371-392.
- Hitzler, L., Janousch, C., Schanz, J., Merkel, M., Heine, B., Mack, F., Hall, W., Ochsner, A., 2017. Direction and location dependency of selective laser melted AlSi10Mg specimens. *J. Mater. Process. Technol.* 243, 48-61.
- Hong, Y., Li, S., Li, H., Li, J., Sun, G., Wang, Y.-D., 2018. Development of intergranular residual stress and its implication to mechanical behaviors at elevated temperatures in AL6XN austenitic stainless steel. *Metall. Mater. Trans. A* 49, 3237-3246.
- Hull, D., Bacon, D.J., 2011. *Introduction to dislocations*, 5th ed. Butterworth-Heinemann.
- Hutchings, M.T., Withers, P.J., Holden, T.M., Lorentzen, T., 2005. *Introduction to the characterization of residual stress by neutron diffraction*, 1st ed. CRC Press, Boca Raton.
- Jiang, F., Masumura, T., Hirata, K., Tsuchiyama, T., Takaki, S., 2019. A new diffraction line profile breadth analysis approach for evaluating plastic lattice strain anisotropy in cold-worked nickel under various strain paths. *Int. J. Plast.* 112, 89-107.
- Kaufman, J.G., Rooy, E.L., 2004. *Aluminum alloy castings: properties, processes and applications*. ASM International.
- Kempen, K., Thijs, L., Van Humbeeck, J., Kruth, J.P., 2012. Mechanical properties of AlSi10Mg produced by selective laser melting. *Phys. Procedia* 39, 439-446.
- Kim, D.K., Hwang, J.H., Kim, E.Y., Heo, Y.U., Woo, W., Choi, S.H., 2017. Evaluation of the stress-strain relationship of constituent phases in AlSi10Mg alloy produced by selective laser

- melting using crystal plasticity FEM. *J. Alloys Compd.* 714, 687-697.
- Kim, J.G., Bae, J.W., Park, J.M., Woo, W., Harjo, S., Chin, K.-G., Lee, S., Kim, H.S., 2019. Synergetic strengthening of layered steel sheet investigated using an in situ neutron diffraction tensile test. *Sci. Rep.* 9, 6829.
- Kocks, U.F., Mecking, H., 2003. Physics and phenomenology of strain hardening: the FCC case. *Prog. Mater. Sci.* 48, 171-273.
- Korsunsky, A.M., Wells, K.E., Withers, P.J., 1998. Mapping two-dimensional state of strain using synchrotron X-ray diffraction. *Scr. Mater.* 39, 1705-1712.
- Kröner, E., 1958. Berechnung der elastischen Konstanten des Vielkristalls aus den Konstanten des Einkristalls. *Zeitschrift Fur Physik* 151, 504-518.
- Li, J.F., Peng, Z.W., Li, C.X., Jia, Z.Q., Chen, W.J., Zheng, Z.Q., 2008. Mechanical properties, corrosion behaviors and microstructures of 7075 aluminium alloy with various aging treatments. *Trans. Nonferrous Met. Soc. China* 18, 755-762.
- Li, W., Li, S., Liu, J., Zhang, A., Zhou, Y., Wei, Q.S., Yan, C.Z., Shi, Y.S., 2016. Effect of heat treatment on AlSi10Mg alloy fabricated by selective laser melting: microstructure evolution, mechanical properties and fracture mechanism. *Mater. Sci. Eng. A* 663, 116-125.
- Li, Z., Li, Z., Tan, Z., Xiong, D.-B., Guo, Q., 2020. Stress relaxation and the cellular structure-dependence of plastic deformation in additively manufactured AlSi10Mg alloys. *Int. J. Plast.* 127, 102640.
- Liang, Z.Y., Wang, X., Huang, W., Huang, M.X., 2015. Strain rate sensitivity and evolution of dislocations and twins in a twinning-induced plasticity steel. *Acta Mater.* 88, 170-179.
- Liu, C.H., Yang, J.S., Ma, P.P., Ma, Z.Y., Zhan, L.H., Chen, K.L., Huang, M.H., Li, J.J., Li, Z.M., 2020. Large creep formability and strength-ductility synergy enabled by engineering dislocations in aluminum alloys. *Int. J. Plast.* 134, 102774.
- Liu, J., To, A.C., 2017. Quantitative texture prediction of epitaxial columnar grains in additive manufacturing using selective laser melting. *Addit. Manuf.* 16, 58-64.
- Maamoun, A.H., Xue, Y.F., Elbestawi, M.A., Veldhuis, S.C., 2019. The effect of selective laser melting process parameters on the microstructure and mechanical properties of Al6061 and AlSi10Mg alloys. *Materials* 12, 12.
- Mughrabi, H., 2016. The α -factor in the Taylor flow-stress law in monotonic, cyclic and quasi-stationary deformations: dependence on slip mode, dislocation arrangement and density. *Curr. Opin. Solid State Mat. Sci.* 20, 411-420.
- Nguyen, T., Luscher, D.J., Wilkerson, J.W., 2019. The role of elastic and plastic anisotropy in

- intergranular spall failure. *Acta Mater.* 168, 1-12.
- Olakanmi, E.O., Cochrane, R.F., Dalgarno, K.W., 2015. A review on selective laser sintering/melting (SLS/SLM) of aluminium alloy powders: processing, microstructure, and properties. *Prog. Mater. Sci.* 74, 401-477.
- Orowan, E., 1940. Problems of plastic gliding. *Proc. Phys. Soc.* 52, 8-22.
- Randau, C., Garbe, U., Brokmeier, H.G., 2011. StressTextureCalculator: a software tool to extract texture, strain and microstructure information from area-detector measurements. *J. Appl. Crystallogr.* 44, 641-646.
- Roters, F., Raabe, D., Gottstein, G., 2000. Work hardening in heterogeneous alloys - a microstructural approach based on three internal state variables. *Acta Mater.* 48, 4181-4189.
- Sahu, P., Shee, S.K., Hamada, A.S., Rovatti, L., Sahu, T., Mahato, B., Chowdhury, S.G., Porter, D.A., Karjalainen, L.P., 2012. Low strain rate deformation behavior of a Cr-Mn austenitic steel at -80 °C. *Acta Mater.* 60, 6907-6919.
- Sallez, N., Boulnat, X., Borbely, A., Bechade, J.L., Fabregue, D., Perez, M., de Carlan, Y., Hennet, L., Mocuta, C., Thiaudiere, D., Brechet, Y., 2015. In situ characterization of microstructural instabilities: recovery, recrystallization and abnormal growth in nanoreinforced steel powder. *Acta Mater.* 87, 377-389.
- Samei, J., Amirmaleki, M., Shirinzadeh Dastgiri, M., Marinelli, C., Green, D.E., 2019. In-situ X-ray tomography analysis of the evolution of pores during deformation of AlSi10Mg fabricated by selective laser melting. *Mater. Lett.* 255, 126512.
- Sauzay, M., Kubin, L.P., 2011. Scaling laws for dislocation microstructures in monotonic and cyclic deformation of fcc metals. *Prog. Mater. Sci.* 56, 725-784.
- Schöbel, M., Baumgartner, G., Gerth, S., Bernardi, J., Hofmann, M., 2014. Microstresses and crack formation in AlSi7MgCu and AlSi17Cu4 alloys for engine components. *Acta Mater.* 81, 401-408.
- Sidor, J.J., Petrov, R.H., Kestens, L.A.I., 2011. Modeling the crystallographic texture changes in aluminum alloys during recrystallization. *Acta Mater.* 59, 5735-5748.
- Song, G., Sun, Z., Li, L., Clausen, B., Zhang, S.Y., Gao, Y., Liaw, P.K., 2017. High temperature deformation mechanism in hierarchical and single precipitate strengthened ferritic alloys by in situ neutron diffraction studies. *Sci. Rep.* 7, 45965.
- Srinivas, B., Panigrahi, S.K., 2020. A phenomenological model based on nanostructured dislocation cluster interactions to predict the work hardening behavior of cryodeformed materials. *Int. J. Plast.* 133, 102772.

- Steuwer, A., Rahman, M., Shterenlikht, A., Fitzpatrick, M.E., Edwards, L., Withers, P.J., 2010. The evolution of crack-tip stresses during a fatigue overload event. *Acta Mater.* 58, 4039-4052.
- Stokes, A.R., 1948. A numerical fourier-analysis method for the correction of widths and shapes of lines on X-ray powder photographs. *Proc. Phys. Soc.* 61, 382-391.
- Takata, N., Kodaira, H., Sekizawa, K., Suzuki, A., Kobashi, M., 2017. Change in microstructure of selectively laser melted AlSi10Mg alloy with heat treatments. *Mater. Sci. Eng. A* 704, 218-228.
- Takeuchi, T., 1975. Work hardening of copper single crystals with multiple glide orientations. *Trans. Jpn. Inst. Met.* 16, 629-640.
- Tang, M., Pistorius, P.C., 2017. Anisotropic mechanical behavior of AlSi10Mg parts produced by selective laser melting. *JOM* 69, 516-522.
- Taylor, G.I., 1934. The mechanism of plastic deformation of crystals. Part I.—Theoretical. *Proc. R. Soc. Lon. Ser. A* 145, 362-387.
- Thijs, L., Kempen, K., Kruth, J.P., Van Humbeeck, J., 2013. Fine-structured aluminium products with controllable texture by selective laser melting of pre-alloyed AlSi10Mg powder. *Acta Mater.* 61, 1809-1819.
- Trevisan, F., Calignano, F., Lorusso, M., Pakkanen, J., Aversa, A., Ambrosio, E.P., Lombardi, M., Fino, P., Manfredi, D., 2017. On the selective laser melting (SLM) of the AlSi10Mg alloy: process, microstructure, and mechanical properties. *Materials (Basel)* 10, 76.
- Ungar, T., Dragomir, I., Revesz, A., Borbely, A., 1999. The contrast factors of dislocations in cubic crystals: the dislocation model of strain anisotropy in practice. *J. Appl. Crystallogr.* 32, 992-1002.
- Ungar, T., Harjo, S., Kawasaki, T., Tomota, Y., Ribarik, G., Shi, Z.M., 2017. Composite behavior of lath martensite steels induced by plastic strain, a new paradigm for the elastic-plastic response of martensitic steels. *Metall. Mater. Trans. A* 48A, 159-167.
- Ungar, T., Ott, S., Sanders, P.G., Borbely, A., Weertman, J.R., 1998. Dislocations, grain size and planar faults in nanostructured copper determined by high resolution X-ray diffraction and a new procedure of peak profile analysis. *Acta Mater.* 46, 3693-3699.
- Ungar, T., Stoica, A.D., Tichy, G., Wang, X.L., 2014. Orientation-dependent evolution of the dislocation density in grain populations with different crystallographic orientations relative to the tensile axis in a polycrystalline aggregate of stainless steel. *Acta Mater.* 66, 251-261.
- Uzan, N.E., Shneck, R., Yeheskel, O., Frage, N., 2017. Fatigue of AlSi10Mg specimens fabricated by additive manufacturing selective laser melting (AM-SLM). *Mater. Sci. Eng. A*

704, 229-237.

Van Petegem, S., Wagner, J., Panzner, T., Upadhyay, M.V., Trang, T.T.T., Van Swygenhoven, H., 2016. In-situ neutron diffraction during biaxial deformation. *Acta Mater.* 105, 404-416.

Wang, D., Ma, Z.Y., 2009. Effect of pre-strain on microstructure and stress corrosion cracking of over-aged 7050 aluminum alloy. *J. Alloys Compd.* 469, 445-450.

Wang, H., Clausen, B., Capolungo, L., Beyerlein, I.J., Wang, J., Tome, C.N., 2016. Stress and strain relaxation in magnesium AZ31 rolled plate: in-situ neutron measurement and elastic viscoplastic polycrystal modeling. *Int. J. Plast.* 79, 275-292.

Wang, L.F., Sun, J., Yu, X.L., Shi, Y., Zhu, X.G., Cheng, L.Y., Liang, H.H., Yan, B., Guo, L.J., 2018. Enhancement in mechanical properties of selectively laser-melted AlSi10Mg aluminum alloys by T6-like heat treatment. *Mater. Sci. Eng. A* 734, 299-310.

Wang, M., Huang, M.X., 2020. Abnormal TRIP effect on the work hardening behavior of a quenching and partitioning steel at high strain rate. *Acta Mater.* 188, 551-559.

Wimpory, R.C., Ohms, C., Hofmann, M., Schneider, R., Youtsos, A.G., 2009. Statistical analysis of residual stress determinations using neutron diffraction. *Int. J. Pressure Vessels Pip.* 86, 48-62.

Withers, P.J., 2004. Depth capabilities of neutron and synchrotron diffraction strain measurement instruments. I. The maximum feasible path length. *J. Appl. Crystallogr.* 37, 596-606.

Withers, P.J., Bhadeshia, H.K.D.H., 2001. Overview - Residual stress part 1 - Measurement techniques. *Mater. Sci. Technol.* 17, 355-365.

Wu, J., Wang, X.Q., Wang, W., Attallah, M.M., Loretto, M.H., 2016. Microstructure and strength of selectively laser melted AlSi10Mg. *Acta Mater.* 117, 311-320.

Xiao, Y.K., Bian, Z.Y., Wu, Y., Ji, G., Li, Y.Q., Li, M.J., Lian, Q., Chen, Z., Addad, A., Wang, H.W., 2019. Effect of nano-TiB₂ particles on the anisotropy in an AlSi10Mg alloy processed by selective laser melting. *J. Alloys Compd.* 798, 644-655.

Xie, Q.G., Lian, J.H., Sidor, J.J., Sun, F.W., Yan, X.C., Chen, C.Y., Liu, T.K., Chen, W.J., Yang, P., An, K., Wang, Y.D., 2020. Crystallographic orientation and spatially resolved damage in a dispersion-hardened Al alloy. *Acta Mater.* 193, 138-150.

Yang, F., Luo, H., Pu, E., Zhang, S., Dong, H., 2018. On the characteristics of Portevin-Le Chatelier bands in cold-rolled 7Mn steel showing transformation-induced plasticity. *Int. J. Plast.* 103, 188-202.

Zhang, C., Zhu, H., Hu, Z., Zhang, L., Zeng, X., 2019. A comparative study on single-laser and

multi-laser selective laser melting AlSi10Mg: defects, microstructure and mechanical properties. *Mater. Sci. Eng. A* 746, 416-423.

Zhang, X.X., Andrä, H., Harjo, S., Gong, W., Kawasaki, T., Lutz, A., Lahres, M., 2021. Quantifying internal strains, stresses, and dislocation density in additively manufactured AlSi10Mg during loading-unloading-reloading deformation. *Mater. Des.* 198, 109339.

Zhang, X.X., Zhang, J.F., Liu, Z.Y., Gan, W.M., Hofmann, M., Andrä, H., Xiao, B.L., Ma, Z.Y., 2020. Microscopic stresses in carbon nanotube reinforced aluminum matrix composites determined by in-situ neutron diffraction. *J. Mater. Sci. Technol.* 54, 58-68.

Zhong, Y., Yin, F., Sakaguchi, T., Nagai, K., Yang, K., 2007. Dislocation structure evolution and characterization in the compression deformed Mn-Cu alloy. *Acta Mater.* 55, 2747-2756.

Zhong, Z.Y., Brokmeier, H.G., Gan, W.M., Maawad, E., Schwebke, B., Schell, N., 2015a. Dislocation density evolution of AA 7020-T6 investigated by in-situ synchrotron diffraction under tensile load. *Mater. Charact.* 108, 124-131.

Zhong, Z.Y., Brokmeier, H.G., Maawad, E., Schell, N., 2015b. In-situ investigation of the anisotropic mechanical behavior of rolled AA 7020-T6 alloy through lattice strain evolution during uniaxial tension. *Mater. Sci. Eng. A* 639, 519-525.

Zhou, P., Liang, Z.Y., Liu, R.D., Huang, M.X., 2016. Evolution of dislocations and twins in a strong and ductile nanotwinned steel. *Acta Mater.* 111, 96-107.

Zhuo, L.C., Wang, Z.Y., Zhang, H.J., Yin, E.H., Wang, Y.L., Xu, T., Li, C., 2019. Effect of post-process heat treatment on microstructure and properties of selective laser melted AlSi10Mg alloy. *Mater. Lett.* 234, 196-200.

Table 1 Typical mechanical properties of the AlSi10Mg alloy manufactured by LPBF and die casting. The original strength and elongation values from literature are rounded to keep one decimal if there are several decimals.

Material	Machine	Laser power, W	Scanning speed, mm/s	Yield strength, MPa	Tensile strength, MPa	Elongation, %	Building direction/condition	References	
AlSi10Mg, LPBF, as-built	SLM 280	300	800	270.0	446.3	8.1	-	(Zhuo et al., 2019)	
	HL	NRD-SLM-500	490	1800	314±6	481±2	3.3±0.2	Horizontal, isolated	(Zhang et al., 2019)
					316±7	471±7	3.0±0.2	Horizontal, overlap	
	EOS M290	370	1300	264±4	452±1	8.6±1.0	Horizontal	(Girelli et al., 2019)	
				247±1	482±1	6.5±0.3	Vertical		
	EOSINT M280	400	1000	241±10	384±16	6±1	Vertical	(Uzan et al., 2017)	
	EOS M280	370	1300	188.5±2.5	274±0	15.3±0.1	Horizontal	(Tang and Pistorius, 2017)	
				183.8±5.8	280.2±2.2	12.2±0.4	Vertical		
Renishaw AM250	400	1000	-	334	3.6	Horizontal	(Wang et al., 2018)		
SLM 250HL	350	1170	300	455	5.4	-	(Chen et al., 2017)		

SLM 250HL	350	1140	322.2 ± 8.1	434.3 ± 10.7	5.3 ± 0.2	-	(Li et al., 2016)
SLM 280HL	350	600-930	241.2 ± 5.7	399.1 ± 7.3	6.5 ± 0.4	Horizontal	(Hitzler et al., 2017)
			208.6 ± 16.9	357.5 ± 19.6	3.2 ± 0.1	Vertical	
Concept Laser M1	200	1400	262	391 ± 6	5.6 ± 0.4	Horizontal	(Kempen et al., 2012)
			247	396 ± 8	3.5 ± 0.6	Vertical	
A360.0, Die casting, as-cast	-	-	165	317	4	-	(Kaufman and Rooy, 2004)

Table 2 Chemical composition of the AlSi10Mg powder.

Element	Al	Si	Mg	Fe	Mn	Ti	Cu	Zn	C	Ni	Pb	Sn
Content (wt.%)	Balance	9.0-11.0	0.20-0.45	0-0.55	0-0.45	0-0.15	0-0.10	0-0.10	0-0.05	0-0.05	0-0.05	0-0.05

Table 3 Macro mechanical properties of the LPBF AlSi10Mg specimens.

Specimen	Yield strength (0.2%), MPa	Tensile strength, MPa	Elongation, %
E1, ex-situ	293.5	485.6	6.4
E2, ex-situ	304.4	500.9	7.3
E3, ex-situ	305.2	500.6	7.2
S1, in-situ	297.2	481.4	5.5
S2, in-situ	284.8	-	-

Table 4 $\{hkl\}$ diffraction elastic moduli and of Poisson's ratios both Al and Si phases.

Phase	hkl	Diffraction elastic moduli			Poisson's ratio
		Measured, normalized	Kröner model, normalized	Kröner model, GPa	Kröner model
Al	111	1.00	1.00	73.09	0.342
	200	0.90	0.92	67.44	0.354
	220	0.97	0.98	71.59	0.345
	311	0.93	0.96	69.99	0.348
Si	111	1.00	1.00	175.32	0.201
	220	0.95	0.95	167.24	0.215
	311	0.85	0.91	159.05	0.229
	422	0.91	0.95	167.24	0.215

Table 5. Maximum lattice strain uncertainties (unit in 10^{-6}) before d0 refinement during the entire loading.

Maximum lattice strain uncertainties, 10^{-6}	Al				Si			
	111	200	220	311	111	220	311	422
Up cake	14.78	12.86	17.16	14.74	248.52	828.33	294.04	727.41
Down cake	14.38	12.51	16.77	14.41	237.61	1078.81	291.74	655.64
LD average	14.58	12.69	16.97	14.58	243.07	953.57	292.89	691.53
Left cake	9.76	31.00	14.23	18.06	248.28	570.72	329.48	842.84
Right cake	10.75	34.33	14.81	19.97	256.12	710.61	332.58	817.83
TD average	10.26	32.67	14.52	19.02	252.20	640.67	331.03	830.34

The definitions of up, down, left, and right cakes are described in Fig. 2(c) and section 2.5.